Full Wavefield Migration of Vertical Seismic Profiling data

Alok Kumar SONI

Full Wavefield Migration of Vertical Seismic Profiling data

Alok Kumar SONI

PROEFSCHRIFT

ter verkrijging van de graad van doctor
aan de Technische Universiteit Delft,
op gezag van de Rector Magnificus prof. ir. K.C.A.M. Luyben,
voorzitter van het College voor Promoties,
in het openbaar te verdedigen
op dinsdag 23 december 2014 om 12:30 uur

Master of Technology in Applied Geophysics,
Indian Institute of Technology Roorkee, India
geboren te Gomia, India.

Dit proefschrift is goedgekeurd door de promotor:
Prof. dr. ir. L.J. van Vliet

en de copromotor:
Dr. ir. D.J. Verschuur

Samenstelling promotiecommissie:

Rector Magnificus,	voorzitter
Prof. dr. ir. L.J. van Vliet,	Technische Universiteit Delft, promotor
Dr. ir. D.J. Verschuur,	Technische Universiteit Delft, copromotor
Prof. dr. ir. A. Gisolf,	Technische Universiteit Delft
Prof. dr. ir. C.P.A. Wapenaar,	Technische Universiteit Delft
Prof. Y. Wang,	Imperial College London
Dr. R. Fletcher,	Schlumberger Gatwick, advisor
Prof. dr. ir. P.M. van den Berg,	Technische Universiteit Delft, reservelid

ISBN 978-94-6295-043-6

SUPPORT
The research for this thesis was financially supported by the Delphi consortium.

Typesetting system: LaTeX.

Printed in The Netherlands by Proefschriftmaken.nl

Dedicated to my parents and wife

Contents

1

Introduction to borehole seismic

1.1 Introduction

In exploration seismology, active man-made sources are used as an input to the earth system and we measure the resulting responses. The response of the earth comprises of reflections, refractions, diffractions and possible noises (both random and coherent noises). For an overview on exploration seismic, see Dobrin and Savit [1988]; Telford et al. [1990]. The objective of the oil and gas exploration industry is to extract reliable, high-resolution structural and stratigraphic details of the prospect area using seismic measurements. The structural and stratigraphic details aid the interpretation geologist, petrophysicist as well as reservoir engineers in understanding the prospect and eventually helps in decision making towards the drilling and production processes.

Surface seismic has been the major exploration tool in the oil and gas industry over the last six decades. Therefore, seismic prospecting has become one of the most dynamic field in terms of innovative research towards a better understanding, of both the acquisition as well as the processing of the data. Vertical Seismic Profiling (VSP) has been one of the important innovations in the data acquisition design. For a detailed introduction to this technology, see Gal'perin [1974]; DiSiena et al. [1981]; Balch et al. [1982]; Hardage [1985]; Hinds et al. [1996]; Pereira and Jones [2010]. Basically, vertical seismic profiling is a borehole seismic technique. As the name suggests, the detectors are placed in a borehole (usually) near the reservoir, while the seismic sources are located near the surface of the earth.

In fact, in seismic measurements, we see all possible geometries such as surface

seismic (Figure 1.1a) with both sources and receivers being located at the surface; vertical seismic profiling (Figure 1.1b) with sources located on the surface and the receivers being located in a borehole; crosshole seismic profiling (Figure 1.1c) with both sources and receivers, being located in different boreholes; and horizontal or deviated well (Figure 1.1d) profiling with the sources located on the surface and the receivers located in a near-horizontal well closer to the reservoir. An example common-shot gather is simulated using a 2D acoustic finite difference method, shown in Figures 1.1e, 1.1f, 1.1g and 1.1h for their corresponding geometries given in Figures 1.1a, 1.1b, 1.1c and 1.1d, respectively.

These different geometries to acquire seismic data meet different exploration objectives. Further, in the past, we have also seen different VSP geometries, such as zero-offset VSP, offset VSP, walkaway VSP, walkabove VSP, salt-proximity VSP, drill-bit VSP and multi-offset VSP. For an overview of these different geometries, see for example Hope et al. [1998]. The VSP geometries vary according to the geological objectives and challenges in the prospecting area [Oristaglio, 1985]. A discussion on various kinds of VSP field geometries is beyond the scope of this thesis.

In this research, our objective is to obtain the best possible image from walkaway VSP data. A walkaway VSP geometry comprises of geophones being located in a vertical or deviated borehole and an array of surface sources in a line moving away from the well. In fact, among different VSP acquisition geometries, walkaway VSP provides a reasonable laterally extended high-resolution image of the reservoir around the well trajectory, see e.g. Payne et al. [1990]. Figure 1.2 shows a schematic diagram of a typical 2D and 3D walkaway VSP geometry in a marine environment.

In the following sections, we will discuss the advantages and the limitations of VSP imaging[1] in current industrial practice, followed by the motivation and proposals of our research and a brief outline of this thesis.

1.2 VSP imaging: advantages and limitations

Over the past two decades, vertical seismic profiling has proven to provide high resolution and reliable images of oil and gas reservoirs around the globe [Arroyo et al., 2003; Müller et al., 2010a,b]. In VSP acquisition, since the receivers are placed

[1] Seismic Imaging: Also called seismic migration. Imaging can be defined as the transformation of seismic data recorded as a function of arrival time into a scaled version of the true geometry of subsurface geologic features that produced the recorded seismic energy. Imaging involves focusing and positioning and depends on a specific earth model. Focusing involves collapsing diffractors, maximizing amplitude, reproducing wavelet character, etc; positioning involves locating events correctly, sharpening event terminations relative to faults, salt flanks, unconformities, etc. [Sherrif, 2002]

5

Application of full wavefield migration to blended VSP data

5.1 Introduction

In the previous chapters, we introduced full wavefield modelling and full wavefield migration (FWM) for walkaway VSP data. In this chapter, we will present the application of FWM in the case of blended source VSP acquisition. In blended source (also called simultaneous source) experiments, more than one shot are fired simultaneously or with a delayed time. The sources may vary in spatial location as well as source strength. Blended source acquisition [Beasley et al., 1998; Ikelle, 2007; Berkhout, 2008; Neelamani et al., 2010] in the surface seismic case is slowly becoming a routine practice in the oil and gas industry. Blending in surface seismic has made huge 3D surveys possible in an economical survey time. It has proven to improve both the quality as well as economic aspects. It reduces the costs of data acquisition and survey time, while still acquiring a dense survey [see for example Berkhout, 2008; Howe et al., 2008; Bouska, 2010; Berkhout et al., 2012; Doulgeris, 2013]. The word 'quality' here indicate the illumination capability of blended source arrays compared to unblended source. For a theoretical discussion, please see Berkhout et al. [2012], where it is described that even for a very simple blending code, e.g., time delays only, the incident wavefield at a particular subsurface grid point is represented by a dispersed time series, corresponding to a complex code. This time series is grid point dependent and contains multi-offset, multi-azimuth information and therefore enhances grid point illumination.

Recently, Gulati et al. [2011] proposed acquiring 3D VSP data using simultaneous sources to reduce the borehole acquisition costs significantly. Note that VSP acquisition is relatively costly because of the fact that all activities need to be stopped (strictly production). Thus, reducing downtime via blended acquisition is of great importance. Nawaz and Borland [2013] discussed the processing sequence for simultaneous source 3D VSP data. In a similar way, Morley [2013] discussed the application of compressed sensing[1] in 3D VSP acquisition and processing.

For the processing, imaging and (full waveform) inversion of the blended data, we have seen methods of deblending sources from the acquired seismic data [for example see Spitz et al., 2008; Moore et al., 2008; Kim et al., 2009; Mahdad et al., 2011, 2012; Beasley et al., 2012; van Borselen et al., 2012; Wapenaar et al., 2012], the result of which can be fed into conventional processing and imaging methods. On the other hand, there have been investigations in performing processing [see Hou et al., 2012; Bagaini et al., 2012], imaging [see Verschuur and Berkhout, 2009; Tang and Biondi, 2009; Jiang and Abma, 2010; Verschuur and Berkhout, 2011; Berkhout et al., 2012; Dai et al., 2012; Huang and Schuster, 2012] and inversion [see Guitton and Diaz, 2012; Choi and Alkhalifah, 2012; Plessix et al., 2012] of the blended seismic data directly without separating the sources or deblending them.

Along this latter approach, we propose full wavefield migration (FWM) to image blended VSP data [Soni and Verschuur, 2013b]. Hence, the least-squares inversion process in FWM can help in estimating the subsurface reflectivity such that it explains the total blended data. In this chapter we describe the extension of the forward modelling algorithm to include blended VSP data. Furthermore, we discuss the potential of FWM in imaging blended VSP data by illustrating some examples using a density-only, synthetic dipping-layer model as well as reservoir-oriented modified Marmousi model. Indeed, we will notice some crosstalk noise in the image due to wavefield interference for blending with high blending factors. However, the blending leakage noise can be reduced by using a constrained least-squares inversion scheme.

[1] Compressed sampling is an alternative subsampling method, different from blending. In compressed sensing, randomized sub-Nyquist sampling is used to capture the structure of the data with the assumption that it is sparse or compressible in some transform domain, such as curvelet domain. For more details on this subject, the readers are referred to Candès and Tao [2006]; Donoho [2006]; Hermann et al. [2012]; Mansour et al. [2012]; Herrmann and Li [2012]. For a discussion on recovery conditions from compressed sensing measurements, see for example Friedlander et al. [2012]. Further discussion on compressed sensing is beyond the scope of this thesis.

5.2 Full wavefield modelling of blended VSP data

To formulate the iterative forward modelling of blended VSP data, we will use similar expressions as in chapter two. In the case of a blended source experiment, we can define the modelling either in its true source-receiver domain or in the reciprocal domain. Let us first define the modelling in the true source-receiver domain. The iterative full wavefield modelling can be formulated in terms of iterative modelling of the total incident wavefields $\vec{P}_{bl}(z_n)$ recursively for all depth levels. The subscript 'bl' represents a blended experiment. The total incident wavefields $\vec{P}_{bl}(z_n)$ comprise a downgoing incident wavefield $\vec{P}^{+}_{bl}(z_n)$ and an upgoing incident wavefield $\vec{P}^{-}_{bl}(z_n)$ at depth level z_n. In the modelling scheme, the first step involves the modelling of the direct downgoing wavefields at all depth levels due to blended source $\vec{S}_{bl}(z_0)$ located at the surface. Thus, the downgoing incident wavefield $\vec{P}^{+}_{bl}(z_n)$, in the first iteration is given by:

$$[\vec{P_{bl}}^{+}(z_n)]^{(1)} \quad = \sum_{m=0}^{n-1} \mathbf{W}^{+}(z_n, z_m)\vec{S_{bl}}^{+}(z_0), \tag{5.2.1}$$

where the superscript (1) indicates the iteration number. Similar as discussed in chapter two, mathematically, the incident wavefield from above, i.e. $\vec{P}^{+}_{bl}(z_n)$, and the one from below, i.e. $\vec{P}^{-}_{bl}(z_n)$, for a given iteration i can be written as:

$$\vec{P}^{+}_{bl}(z_n)^{(i)} \quad = \sum_{m=0}^{n-1} \mathbf{W}^{+}(z_n, z_m)[\delta\vec{P}_{bl}(z_m)^{(i-1)} + \vec{S}^{+}_{bl}(z_0)], \tag{5.2.2}$$

$$\vec{P}^{-}_{bl}(z_n)^{(i)} \quad = \sum_{m=n+1}^{N} \mathbf{W}^{-}(z_n, z_m)\delta\vec{P}_{bl}(z_m)^{(i-1)}, \tag{5.2.3}$$

where the two-way scattered wavefield $\delta\vec{P}_{bl}(z_n)$ can be written as:

$$\delta\vec{P}_{bl}(z_n) = \begin{bmatrix}\mathbf{R}^{\cup}(z_n) & \mathbf{R}^{\cap}(z_n)\end{bmatrix}\begin{bmatrix}\vec{P}^{+}_{bl}(z_n) \\ \vec{P}^{-}_{bl}(z_n)\end{bmatrix} = \mathbf{R}(z_n)\vec{P}_{bl}(z_n). \tag{5.2.4}$$

Here, the blended source vector $\vec{S}^{+}_{bl}(z_0)$ can be defined using the complete or full source matrix at the surface $\mathbf{S}(z_0)$ and a blending operator $\vec{\Gamma}_{bl}(z_0)$ [see Berkhout, 2008] as:

$$\vec{S}^{+}_{bl}(z_0) = \mathbf{S}^{+}(z_0)\vec{\Gamma}_{bl}(z_0), \tag{5.2.5}$$

where the blending operator $\vec{\Gamma}_{bl}(z_0)$ can be written as $\vec{\Gamma}_{bl}(z_0) = [\gamma_1, \gamma_2, \gamma_3, ..., \gamma_N]$, with $\gamma_n = a_n e^{-j\omega T_n}$. In this case, T_n is a random time-shift applied to blend the sources and a_n is a scale factor that can be $a_n = 0$ for those sources not included in the blended experiment. We will use the term 'blending factor' to define the number of shots blended together i.e. number of $a_n \neq 0$. We will use the term

scheme, the upgoing wavefield at the surface $\vec{P}_{bl}^{-}(z_0)$ is equivalent to the modelled surface seismic data. Now, for walkaway VSP data modelling, we can select the upgoing and downgoing wavefields for all the spatial locations i.e. both lateral and vertical location where the receivers are present. The modelled VSP data is obtained by taking the sum of the upgoing and downgoing wavefields measured in the borehole receivers.

Above, we discussed the modelling for a blended source experiment in the true source-receiver domain. As mentioned earlier, we can also define the modelling in the reciprocal domain, which gives an equivalent blended data. In the inversion scheme, we perform modelling in the reciprocal domain (discussed in detail in later sections). The important point to note here is that in the reciprocal domain, we assume unblended sources in the borehole (all corresponding to true receiver locations) and estimate the unblended modelled data for receivers located on the surface (same as described in chapter two). After each iteration, we perform the receiver-side blending to obtain the equivalent blended data. Note that the receiver-side blending can be done using the transpose of the same operator used in data acquisition.

In data matrix notations (for one frequency component), $\mathbf{P}_{vsp}$ and $\mathbf{P}_{vsp,bl}$ represents unblended and blended VSP data, respectively. A column-vector and a row-vector of these matrices represents a common-source gather and a common-receiver gather, respectively. In the reciprocal domain, the data matrices are represented by $\mathbf{P}_{vsp}^{T}$ and $\mathbf{P}_{vsp,bl}^{T}$ (transpose of the original matrices), where a column-vector and a row-vector of the matrices now represents a common-receiver gather and a common-source gather, respectively. Furthermore, in terms of matrix multiplication, blending operator Γ_{bl} when act on the right side of the data matrix $\mathbf{P}_{vsp}$, it is equivalent to source-side blending. While, in the reciprocal domain, when the transposed blending operator Γ_{bl}^{T} act on the left side of the reciprocal domain data matrix $\mathbf{P}_{vsp}^{T}$, it indicates the receiver-side blending [Soni and Verschuur, 2014b]. Figure 5.2 schematically illustrates this relationship. Please see the caption for specifications.

5.3 Numerical examples of the forward modelling

In order to illustrate the modelling scheme, we used a synthetic density model (with constant velocity, same as used in chapter two, shown in Figure 2.10). Figure 5.3 shows the density model and the corresponding scalar reflectivity model used to illustrate full wavefield modelling for blended source experiments. To illustrate, the models are annotated schematically with a blended source experiment located at the surface and the receivers being located in a borehole. For the conventional (unblended) acquisition geometry, the sources are located at the surface between $0m$ to $3000m$, laterally, at a spacing of $20m$ (i.e. we have 151

5.4 Full wavefield migration of blended VSP data

In the previous section we discussed how to incorporate the blended source experiments to model VSP data in the true source domain, followed by selection of the total wavefields at the known receiver's spatial locations. However, we propose to perform the imaging in the common-receiver domain, similar as for the unblended VSP data, that was discussed extensively in chapter three. For the blended VSP data, it is impossible to perform the imaging in the common-receiver domain, because the common-receiver gathers show random events [see also Mahdad, 2012; Doulgeris, 2013]. Therefore, to circumvent this problem, pseudo-blending is included as part of the imaging scheme. We believe that doing the full deblending (active deblending) followed by FWM will give a similar result in quality, compared to simultaneous deblending (passive deblending[2]) and migration in FWM. For conventional migration, this has been discussed in Gulati et al. [2011]. But these strategies are still a subject of further research. The active deblending becomes more and more difficult with increasing blending factors due to large null-space or leakage subspace[3]. For detailed discussion on this, please see Doulgeris et al. [2012]; Doulgeris [2013]. On the other hand, because imaging the blended data is also highly-underdetermined problem and suffer from a large null-space, therefore a constrained least-squares inversion based imaging algorithm can help in reducing the blending crosstalk, and hence reducing the null-space of the problem. Therefore, we can say that simultaneous deblending and imaging makes the algorithm more efficient and robust. In other words, the FWM scheme actually acts as a deblending algorithm.

Figure 5.11 shows a generalized block diagram for the inversion scheme in FWM for blended VSP data. This is similar to Figure 3.1 with two intermediate steps added, being pseudo-deblending of the data residual and blending of the estimated data.

Again, the migration is performed as a feedback process. In order to perform the migration in the common-receiver domain, we need to apply an intermediate step of pseudo-deblending to the data residual in the feedback loop. Note that the intermediate pseudo-deblended is imaged, yielding a subsurface reflectivity that is used to simulate the response using full wavefield modeling (in the reciprocal domain), which is subsequently blended by the same blending operator used in data acquisition. The estimated blended data is compared with the measured blended data. The residual of the measured and simulated data, after

[2]Passive deblending: Passive deblending is same as pseudo-deblending. Pseudo-deblending is basically finding the generalized inverse of the blending matrix.

[3]Null-space or leakage subspace: In leakage subspace, the vectors corresponds to energy that is coherent for more than one source contributing to the same blended experiment and therefore, this energy cannot be assigned uniquely to one particular source. For a geometrical interpretation of data and model null-space in linear algebra, see Strang [2003]

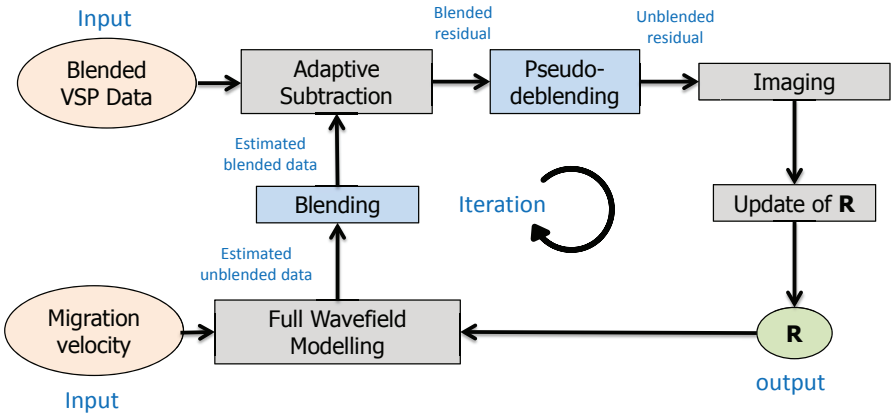

Figure 5.11: *Block diagram (similar to Figure 3.1), FWM for blended VSP data, showing the general feedback loop for inversion in the common-receiver domain. The intermediate pseudo-deblended data is imaged, yielding subsurface reflectivity. The estimated reflectivity is used to simulate the response using full wavefield modelling (in the reciprocal domain) and then blended by the same blending operator used in data acquisition. The blended estimated data is compared with the measured blended data. The residual of the measured and simulated data after adaptive subtraction is fed back in the loop to update the reflectivity iteratively. Each iteration adds or uses a higher order of multiples.*

adaptive subtraction, is fed back in the loop to update the reflectivity iteratively. Note that in FWM, each iteration adds and uses a higher order of multiples. Since, the migration is performed as a feedback process, the first iteration is similar to conventional imaging of the primary wavefields. Next, each iteration of FWM involves an iteration of full wavefield modeling, and hence, adds or uses a higher order of multiples to estimate the reflectivity. With subsequent iterations of FWM, the image becomes more accurate and sharper, i.e. the vertical resolution increases and the full-wavefield is better explained. This is the same as in other least-squares imaging schemes: with subsequent iterations, the estimated reflectivity converges to a reasonable solution. However, in addition, in FWM, with each additional iteration also the higher-order scattering effects in the data are explained. Hence, the first iteration is equivalent to conventional imaging of the primary wavefields of pseudo-deblended data containing blending interference noise.

Pseudo-deblending is basically finding the generalized inverse of the blending matrix [see also Mahdad, 2012; Doulgeris, 2013]. Mathematically, if the blended VSP data matrix, for one frequency component is written as:

$$\mathbf{P}_{vsp,bl} = \mathbf{P}_{vsp}\Gamma_{bl}, \tag{5.4.7}$$

Furthermore, similar as discussed in chapter three, the reflectivity image obtained in the first iteration is used to simulate the response using full wavefield modelling in the reciprocal domain. The simulated data gives the wavefields for the equivalent receivers at the surface in the reciprocal domain, where the locations resemble the location of unblended sources in the observed data. In order to compare the simulated data to the blended data, we apply blending to the simulated data using the same operator as used in data acquisition. Please note here that the modelling scheme discussed in the previous sections for the blended sources at the surface for true domain VSP data is equivalent to the two steps in this inversion block diagram. They are the full wavefield modelling in the reciprocal domain to simulate unblended data at the surface (which is geometrically equivalent to the true unblended data in the common-receiver domain) plus equivalent receiver-blending in the reciprocal domain. Figure 5.2 illustrated this relationship using the simple matrix identity, where Figure 5.2a schematically shows source-side blending to get a blended VSP data matrix and Figure 5.2b shows that the transpose of equation (5.4.7) is also true, i.e. it is equivalent to receiver-side blending for common-receiver data.

As Figure 5.11 shows, the residual after least-squares subtraction or adaptive subtraction of the simulated blended data and the measured blended data are subjected to pseudo-deblending, after which it is used to update the reflectivity, iteratively, in such a way that the data residual is minimized. Again, note that each iteration of FWM involves a round-trip iteration of full wavefield modelling, and hence, uses a higher order of multiples to estimate the reflectivity.

Similar to the optimization scheme discussed in chapter three, imaging blended VSP data using FWM is also defined as an optimization problem, where the simulation of the data is compared to the measured or observed data. We can write the objective function J to minimize in a least-squares sense as:

$$J = min \sum_{k} \sum_{\omega} ||\vec{P}^{-}_{bl,obs,k} - \vec{P}^{-}_{bl,est,k}||^2_2, \tag{5.4.10}$$

where $\vec{P}^{-}_{bl,obs,k}(z_0)$ and $\vec{P}^{-}_{bl,est,k}(z_0)$ are the observed and estimated blended VSP data due to the k^{th} blended source term. Note that the estimated blended VSP data is a function of the reflectivity matrix $\mathbf{R}$. Basically, to simulate data using full wavefield modelling at the surface due to the l^{th} source $\vec{S}_l$ in the borehole in the reciprocal domain can be written as:

$$\vec{P}^{-}_{l}(z_0) = \sum_{m=0}^{N} \mathbf{W}^{-}(z_0, z_m)[\mathbf{R}(z_j)\vec{P}_l(z_m) + \vec{S}^{-}_{l}(z_m)]. \tag{5.4.11}$$

After modelling of the data in the reciprocal domain, the receiver-side blending is performed in the common-receiver domain as:

$$\mathbf{P}^{T}_{vsp,bl} = \Gamma^{T}_{bl}\mathbf{P}^{T}_{vsp}. \tag{5.4.12}$$

The k^{th} row of the data matrix $\mathbf{P}^T_{vsp,bl}$ is equivalent to the estimated blended common-source gather $\vec{P}^-_{bl,est,k}(z_0)$. Note again that in the acoustic approximation, we can write $\mathbf{R}^{\cap}(z_n) = -\mathbf{R}^{\cup}(z_n)$. This reduces the number of parameters to estimate in the inversion from two reflectivity matrices per depth level ($\mathbf{R}^{\cap}$, $\mathbf{R}^{\cup}$) to one ($\mathbf{R}^{\cup}$).

The least-squares inversion for blended VSP data suffers from blending noise leaking into the image space especially for higher blending factors. So, in order to suppress the blending noise leaking into the image, we could use a sparsity-promoting constraint in the inversion scheme, similar to what was done in chapter three. Hence, the new objective function for the constrained least-squares inversion can be written as:

$$J = \sum_k \sum_\omega ||\vec{P}^-_{bl,obs,k} - \vec{P}^-_{bl,est,k}||_2^2 + \epsilon^2 F(\mathbf{R}), \tag{5.4.13}$$

where, $F(\mathbf{R})$ is a sparsity-promoting norm imposed on the reflectivity and ϵ^2 is a weighting parameter that governs the trade-off between the data misfit and the model prior usually depending on the noise content of the data. Note again, the subscript k is for the k^{th} blended source. For the numerical examples ahead, we have used the Cauchy norm (same as in chapter three), that is defined as:

$$F(\mathbf{R}) = \sum_n \sum_j log(1 + \frac{R^2_{jj,n}}{\sigma_r^2}), \tag{5.4.14}$$

where $R_{jj,n}$ is a sample of the reflectivity image at lateral location j (i.e. a diagonal element from matrix $\mathbf{R}(z_n)$) and σ_r is the weighting parameter in the Cauchy norm. The above optimization problem can be solved by an iterative optimization scheme in the same way as discussed in chapter three, to estimate the reflectivity of the subsurface. In Table 5.1, the pseudo-code of the FWM inversion algorithm for blended VSP data using conjugate gradient scheme is given.

5.5 Numerical examples of FWM for blended VSP data

To illustrate the FWM inversion scheme, we have modelled VSP data using an acoustic 2D finite-difference method, with the full source geometry (conventional geometry) and using the density model as shown in Figure 5.3a. The unblended VSP data are simulated for uniformly distributed sources, laterally located between $0m$ and $3000m$, with a source spacing of $20m$, at the surface. The receivers are located between a depth of $100m$ to $1000m$, at a depth spacing of $10m$. The simulated unblended VSP data were then numerically blended by adding shots with random time shifts. In order to test the imaging process for the blended

PSEUDO-CODE

- initialization: $\mathbf{R}^{(0)} = 0$, $\vec{E}_{bl,k} = \vec{P}^{T}_{bl,obs,k}, i = 1$

- while $i \leq i_{max}$ or $|\vec{E}_{bl,k}| < |\vec{E}_{tolerance}|$
  - compute $\vec{P}^{+(i)}_{k}$, $\vec{P}^{-(i)}_{k}$ for all sources k, at all depth levels
  - estimate unblended $\vec{P}^{T}_{est,k}$ at the surface
  - blend the estimated data at the surface $\vec{P}^{T}_{est,k} = \Gamma^{T}_{bl}\vec{P}^{T}_{est,k}$
  - blended data misfit $\vec{E}_{bl,k} = \vec{P}^{T}_{bl,obs,k} - \vec{P}^{T}_{bl,est,k}$
  - pseudo-deblended data misfit $\vec{E}_{k} = \frac{1}{b}\vec{E}_{k}\Gamma^{H}_{bl}$
  - compute gradient $\Delta\mathbf{R}^{\cup(i)}$ for all depth levels
    if $i = 1$
    $\beta^{(i)} = 0$
    else
    $\beta^{(i)} = \Delta\mathbf{R}^{(i)H}[\Delta\mathbf{R}^{(i)} - \Delta\mathbf{R}^{(i-1)}]/[\Delta\mathbf{R}^{(i-1)H}\Delta\mathbf{R}^{(i-1)}]$
  - estimate conjugate direction, $\Delta\mathbf{R}^{\cup(i)}_{cg} = \Delta\mathbf{R}^{\cup(i)} + \beta^{(i)}\Delta\mathbf{R}^{\cup(i-1)}_{cg}$
  - search for $\alpha^{(i)}$, $\alpha^{(i)} = argmin_{\alpha}[J(\mathbf{R}^{\cup(i-1)} + \alpha^{(i)}\Delta\mathbf{R}^{\cup(i)}_{cg})]$
  - update reflectivity matrix, $\mathbf{R}^{(i)} = \mathbf{R}^{(i-1)} + \alpha^{(i)}\Delta\mathbf{R}^{\cup(i)}_{cg}$
  - $i = i + 1$

Table 5.1: *Pseudo-code for the full wavefield migration algorithm using an iterative conjugate-gradient scheme to image blended VSP data in common-receiver domain.*

data, we did the numerical blending by adding shots with random time shifts, the number of shots added to make one blended shot is defined by the 'blending factor'. We have tested the scheme for blending factor one, two, three and four. Figure 5.16 shows snapshots of the wavefield propagation in the finite-difference modeling for numerically blended shot experiments with blending factors one, two and three.

Figures 5.17, 5.18, 5.19 and 5.20 illustrate schematically the numerical blending process, showing a frequency slice of the blending operator Γ_{bl}, an example of the common-shot and common-receiver gathers after numerical blending for blending factor one, two, three and four, respectively. Specifically, Figures 5.17a, 5.18a, 5.19a and 5.20a show an example of an unblended common-shot gather and Figures 5.17b, 5.18b, 5.19b and 5.20b show a frequency slice of the corresponding blending operator, with blending factor one, two, three and four respectively. Figures 5.17c, 5.18c, 5.19c and 5.20c show an example of a blended common-source

for blended VSP data as a strategy require further research and will depend on the measured data. In this chapter, we propose the latter, to perform FWM on blended VSP data in the common-receiver domain. Hence the algorithm works for simultaneous deblending and imaging, and estimating the subsurface reflectivity such that the modelled data fits the true blended data in a least-square sense.

The estimation of the source wavefield is highly dependent on how well we can pick the direct arrivals in the measured VSP data. However, picking direct arrivals on blended data directly is challenging. The direct arrivals for blended data can be picked effectively after applying pseudo-deblending. Furthermore, in this paper, we have demonstrated examples from an offshore environment. A similar technique can be extended to use VSP data acquired onshore. However, in land data, there will be other processing aspects to be taken care of such as near-surface issues and statics. A detailed discussion on these issues are beyond the scope of this chapter. We have shown simple synthetic examples to illustrate the imaging of blended VSP data, with different blending factors. Again, using the full wavefield helps to get a significant improvement in the illumination in the images compared to conventional approaches. Note also that, using a constrained inversion scheme does help in reducing the blending interference noise in the image space. Furthermore, we expect that designing the acquisition geometry with optimum blending parameters will also help in reducing the blending noise in the image space. In this chapter, we have not included the concept of compressed sensing in acquiring VSP data and estimating images, however, it is certainly an interesting subject for future research.

Finally, in this research, for 2D VSP data, we found that doing one iteration of modelling followed by one iteration of inversion in the feedback loop lead to converge the algorithm smoothly and yield a reasonably good result. However, for 3D blended surface seismic or OBC (Ocean-bottom cable) data, this strategy may not always work. Hence, for practical cases, one must test strategies like multiple iteration of modelling followed by one iteration of inversion or vice-versa.

6

Elastic FWM: incorporating converted waves in multicomponent VSP data

6.1 Introduction to multi-component VSP data

In practice, VSP data are mostly multi-component records, i.e. the geophones in the borehole can register the x-, the y- and the z- component of the wavefields. Hence, shear-waves or converted waves play a major role in VSP data processing, imaging and interpretation. The P-waves and S-waves have different wave properties, such as the particle velocity and particle direction, which in fact aids in providing additional stratigraphical as well as structural information of the subsurface. Compared to surface seismic data, it is easier to identify the reflected and transmitted primaries and multiples of the converted wavefield in VSP data and, thus, it helps in deriving reliable information about the subsurface lithological properties. Assuming a horizontally layered earth, the location of P-P and P-S reflection points in the VSP geometry are curved and P-S reflection points are displaced toward the receivers, see Figure 6.1, after Stewart et al. [2002]. The P-P and P-S reflection point trajectories are computed for an offset source located $3000m$ away from a vertical well, for a given horizontally layered elastic medium obeying Snell's law. Furthermore, in practice, P-S images have higher spatial resolution than the associated P-P sections from VSP data [see, for example, in Stewart et al., 2002].

In the past, several example applications of multi-component VSP data are dis-

With VSP data acquisition, the orientation of the geophones in the borehole are generally not aligned to the referenced x-, y- and z- direction. Hence, in terms of the processing of multi-component VSP data, one of the major steps is a rotation correction applied to the transverse and vertical component wavefields. After the correction, the recorded three component wavefield are oriented to the referenced x-, y- and z- directions. A subsequent P-S wavefield mode-separation is applied to separate P waves and S waves. We will not discuss the details of P and S wavefield mode-separation in this thesis. For examples in literature, please refer to methods discussed in Dankbaar [1987], Hermann and Wapenaar [1992], Leaney [1990], Blias [2008], Sun et al. [2009], Lou et al. [2013] and Palacios et al. [2013].

We assume to have a P-S mode-separated wavefield from VSP data. So towards elastic FWM, the next step is to incorporate the simulation of converted waves in the full wavefield modelling. In the previous chapters, we have discussed full wavefield modelling and full wavefield migration (FWM) for VSP data in an acoustic scenario, where we assumed the S-wave velocity to be zero, yielding no effect of converted wavefields and angle-dependent effects due to S-wave velocities. An example in section 4.3 does show the effect of non-zero S-wave velocity on $\mathbf{R}_{pp}$ imaging (acoustic imaging), where the observed P-wave data contains converted waves and also shows angle-dependent reflection effects. In the next section, we will extend the concept of acoustic full wavefield modelling to elastic multicomponent full wavefield modelling for VSP data. In the subsequent sections, we will discuss an approach to incorporate the converted waves in imaging.

6.2 Elastic full wavefield modelling: mathematical formulation

In the past, we have seen some examples of elastic multi-component VSP modelling in the literature. Some of the examples are mentioned in chapter two of this thesis, such as the reflectivity method discussed in Mallick and Frazer [1988] and the state-space algorithm discussed in Aminzadeh and Mendel [1985]; Ferber [1988]; Xu [1990]. Also, Young et al. [1984] presented a comparative study of modelling algorithms based on geometric ray theory, asymptotic ray theory, generalized ray theory, Kirchhoff wave theory, Fourier synthesis, finite differences, and finite elements to simulate elastic VSP data. Dietrich and Bouchon [1985] discussed modelling of VSP in elastic media using a discrete wavenumber method [Bouchon and Aki, 1977].

In chapter two of this thesis, we introduced the concept of iterative full wavefield modelling and illustrated examples in the 2D acoustic case. In this section, we will extend the concept of the full wavefield modelling scheme to include the converted wavefields. In order to discuss the mathematical formulation, we will use a similar matrix-vector notation as introduced earlier in chapter two of this thesis. To

account for converted waves, we have to define the continuity boundary condition of both P- and S-wavefields at an interface. Note that P and S-wavefields are the P-wave potential and S-wave potential (Lame potentials) represented by ϕ and $\vec{\psi}$, respectively [for details, please refer to Wapenaar and Berkhout, 1989]. For an isotropic homogeneous elastic medium, the P-wave and S-wave potentials are related to the particle velocities $\vec{v}_p$ and $\vec{v}_s$ and can be written as:

$$\begin{aligned} \vec{v}_p &= \nabla\phi, \\ \vec{v}_s &= \nabla \times \vec{\psi}. \end{aligned} \tag{6.2.1}$$

The total particle velocity is given by $\vec{v} = \vec{v}_p + \vec{v}_s$, and related to the P- and S-wave potentials by (Newton's law):

$$\frac{\partial \vec{v}}{\partial t} = -\frac{1}{\rho}[\nabla\phi + \nabla \times \vec{\psi}]. \tag{6.2.2}$$

Figure 6.3 schematically shows the upgoing and downgoing P- and S- wavefields across a discontinuity at depth level z_n. The upgoing wavefields have a superscript '-' and the the downgoing wavefields have a superscript '+'. Also, similar to chapter two, the wavefields that are incident to a depth level are represented by a vector $\vec{P}$ and the wavefield that are leaving a depth level are represented by a vector $\vec{Q}$. Further, to specify the mode of the wavefield, subscript P and S are used to represent P-waves and S-waves.

Hence, the upgoing and the downgoing P-wavefields just above the discontinuity are represented by $\vec{Q}_p^-$ and $\vec{P}_p^+$, respectively, and the ones just below the discontinuity are represented by $\vec{P}_p^-$ and $\vec{Q}_p^+$, respectively. Similarly, the upgoing and the downgoing S-wavefields just above the discontinuity are represented by $\vec{Q}_s^-$ and $\vec{P}_s^+$, respectively, and the ones just below the discontinuity are represented by $\vec{P}_s^-$ and $\vec{Q}_s^+$, respectively. Now, in order to incorporate the converted wavefields, we will define the reflectivity and transmissivity matrices with subscripts representing the mode of the incident and the corresponding reflected or transmitted wavefields. In such notation, $\mathbf{R}_{pp}^{\cup}$ and $\mathbf{R}_{pp}^{\cap}$ represent reflectivity matrices related to the discontinuity for an incident and reflected P-wavefield, incident from above and below the depth level, respectively (as shown in Figure 6.3b). $\mathbf{R}_{ss}^{\cup}$ and $\mathbf{R}_{ss}^{\cap}$ represent reflectivity matrices related to the discontinuity for an incident and reflected S-wavefield, incident from above and below the depth level, respectively (as shown in Figure 6.3c). $\mathbf{R}_{ps}^{\cup}$ and $\mathbf{R}_{ps}^{\cap}$ represent reflectivity matrices related to the discontinuity for an incident S-wavefield but reflected P-wavefield, incident from above and below the depth level, respectively (as shown in Figure 6.3d). Similarly, $\mathbf{R}_{sp}^{\cup}$ and $\mathbf{R}_{sp}^{\cap}$ represent reflectivity matrices related to the discontinuity for an incident P-wavefield but reflected S-wavefield, incident from above and below the depth level, respectively (as shown in Figure 6.3e). $\mathbf{T}_{pp}^{+}$, $\mathbf{T}_{ss}^{+}$, $\mathbf{T}_{ps}^{+}$, $\mathbf{T}_{sp}^{+}$,

$\mathbf{T}^-_{pp}$, $\mathbf{T}^-_{ss}$, $\mathbf{T}^-_{ps}$, $\mathbf{T}^-_{sp}$ represents the corresponding transmissivity matrices as shown in Figures 6.3b, 6.3c, 6.3d and 6.3e. Note that '+' and '−' signs represents the transmission for downgoing and upgoing wavefields, respectively.

We will define the boundary conditions using the wavefield continuity equations as introduced in Claerbout [1976] [see also Frasier, 1970; Aminzadeh and Mendel, 1982; Berkhout, 2012].

Using the wavefields as well as the reflectivity and the transmissivity matrices notation as discussed above, and as shown in Figure 6.3, the full wavefield relations from the continuity relationship become:

$$\vec{Q}^+_p = \mathbf{T}^+_{pp}\vec{P}^+_p + \mathbf{T}^+_{ps}\vec{P}^+_s + \mathbf{R}^\cap_{pp}\vec{P}^-_p + \mathbf{R}^\cap_{ps}\vec{P}^-_s, \tag{6.2.3}$$

$$\vec{Q}^+_s = \mathbf{T}^+_{sp}\vec{P}^+_p + \mathbf{T}^+_{ss}\vec{P}^+_s + \mathbf{R}^\cap_{sp}\vec{P}^-_p + \mathbf{R}^\cap_{ss}\vec{P}^-_s, \tag{6.2.4}$$

$$\vec{Q}^-_p = \mathbf{R}^\cup_{pp}\vec{P}^+_p + \mathbf{R}^\cup_{ps}\vec{P}^+_s + \mathbf{T}^-_{pp}\vec{P}^-_p + \mathbf{T}^-_{ps}\vec{P}^-_s, \tag{6.2.5}$$

$$\vec{Q}^-_s = \mathbf{R}^\cup_{sp}\vec{P}^+_p + \mathbf{R}^\cup_{ss}\vec{P}^+_s + \mathbf{T}^-_{sp}\vec{P}^-_p + \mathbf{T}^-_{ss}\vec{P}^-_s. \tag{6.2.6}$$

The above equations can be written as a matrix equation given by:

$$\begin{bmatrix} \vec{Q}^+_p \\ \vec{Q}^+_s \\ \vec{Q}^-_p \\ \vec{Q}^-_s \end{bmatrix} = \begin{bmatrix} \mathbf{T}^+_{pp} & \mathbf{T}^+_{ps} & \mathbf{R}^\cap_{pp} & \mathbf{R}^\cap_{ps} \\ \mathbf{T}^+_{sp} & \mathbf{T}^+_{ss} & \mathbf{R}^\cap_{sp} & \mathbf{R}^\cap_{ss} \\ \mathbf{R}^\cup_{pp} & \mathbf{R}^\cup_{ps} & \mathbf{T}^-_{pp} & \mathbf{T}^-_{ps} \\ \mathbf{R}^\cup_{sp} & \mathbf{R}^\cup_{ss} & \mathbf{T}^-_{sp} & \mathbf{T}^-_{ss} \end{bmatrix} \begin{bmatrix} \vec{P}^+_p \\ \vec{P}^+_s \\ \vec{P}^-_p \\ \vec{P}^-_s \end{bmatrix}. \tag{6.2.7}$$

Rearranging the above equation in order to formulate the outgoing wavefields at the interface - $\vec{Q}^+_p$, $\vec{Q}^+_s$, $\vec{Q}^-_p$ and $\vec{Q}^-_s$ as a sum of their corresponding incident wavefields $\vec{P}^+_p$, $\vec{P}^+_s$, $\vec{P}^-_p$ and $\vec{P}^-_s$, respectively and the corresponding two-way scattered terms, we get:

$$\begin{bmatrix} \vec{Q}^+_p \\ \vec{Q}^+_s \\ \vec{Q}^-_p \\ \vec{Q}^-_s \end{bmatrix} = \begin{bmatrix} \vec{P}^+_p + \delta\vec{P}^+_p \\ \vec{P}^+_s + \delta\vec{P}^+_s \\ \vec{P}^-_p + \delta\vec{P}^-_p \\ \vec{P}^-_s + \delta\vec{P}^-_s \end{bmatrix}, \tag{6.2.8}$$

where $\delta\vec{P}^+_p$, $\delta\vec{P}^+_s$, $\delta\vec{P}^-_p$ and $\delta\vec{P}^-_s$ are the scattered downgoing P wavefield, scattered downgoing S wavefield, scattered upgoing P wavefield and scattered upgoing S wavefield, respectively. These scattered wavefields are given by:

$$\begin{bmatrix} \delta\vec{P}_p^{+} \\ \delta\vec{P}_s^{+} \\ \delta\vec{P}_p^{-} \\ \delta\vec{P}_s^{-} \end{bmatrix} = \begin{bmatrix} \mathbf{T}_{pp}^{+} - 1 & \mathbf{T}_{ps}^{+} & \mathbf{R}_{pp}^{\cap} & \mathbf{R}_{ps}^{\cap} \\ \mathbf{T}_{sp}^{+} & \mathbf{T}_{ss}^{+} - 1 & \mathbf{R}_{sp}^{\cap} & \mathbf{R}_{ss}^{\cap} \\ \mathbf{R}_{pp}^{\cup} & \mathbf{R}_{ps}^{\cup} & \mathbf{T}_{pp}^{-} - 1 & \mathbf{T}_{ps}^{-} \\ \mathbf{R}_{sp}^{\cup} & \mathbf{R}_{ss}^{\cup} & \mathbf{T}_{sp}^{-} & \mathbf{T}_{ss}^{-} - 1 \end{bmatrix} \begin{bmatrix} \vec{P}_p^{+} \\ \vec{P}_s^{+} \\ \vec{P}_p^{-} \\ \vec{P}_s^{-} \end{bmatrix}. \quad (6.2.9)$$

First, let us define the convention for one-way wavefield extrapolation between consecutive depth levels. Figure 6.4a and 6.4c show the downgoing P- and S-wavefield $\vec{Q}_p^{+}(z_{n-1})$ and $\vec{Q}_s^{+}(z_{n-1})$ from just below depth level z_{n-1} propagated down to depth level z_n using the propagation operator $\mathbf{W}_p^{+}(z_n, z_{n-1})$ and $\mathbf{W}_s^{+}(z_n, z_{n-1})$, and represented by the downgoing P- and S-wavefield $\vec{P}_p^{+}(z_n)$ and $\vec{P}_s^{+}(z_n)$ just above depth level z_n, respectively.

Similarly, Figure 6.4b and 6.4d show the upgoing P- and S-wavefield $\vec{Q}_p^{-}(z_{n+1})$ and $\vec{Q}_s^{-}(z_{n+1})$ from just above depth level z_{n+1} propagated up to depth level z_n using the propagation operator $\mathbf{W}_p^{-}(z_n, z_{n+1})$ and $\mathbf{W}_s^{-}(z_n, z_{n+1})$, and represented by the upgoing P- and S-wavefield $\vec{P}_p^{-}(z_n)$ and $\vec{P}_s^{-}(z_n)$ just below depth level z_n, respectively. The propagation operators $\mathbf{W}_p$ and $\mathbf{W}_s$ are the phase-shift operators, implemented as space-frequency domain convolution operators that can be calculated using inhomogeneous P- and S-wave background velocity models [Thorbecke et al., 2004]. Mathematically, we can write the one-way P- and S-wavefield propagation for downward propagation as:

$$\vec{P}_p^{+}(z_n) = \mathbf{W}_p^{+}(z_n, z_{n-1})\vec{Q}_p^{+}(z_{n-1}), \quad (6.2.10)$$

$$\vec{P}_s^{+}(z_n) = \mathbf{W}_s^{+}(z_n, z_{n-1})\vec{Q}_s^{+}(z_{n-1}), \quad (6.2.11)$$

and for upward propagation as:

$$\vec{P}_p^{-}(z_n) = \mathbf{W}_p^{-}(z_n, z_{n+1})\vec{Q}_p^{-}(z_{n+1}), \quad (6.2.12)$$

$$\vec{P}_s^{-}(z_n) = \mathbf{W}_s^{-}(z_n, z_{n+1})\vec{Q}_s^{-}(z_{n+1}). \quad (6.2.13)$$

For a detailed derivation of the extrapolation of the elastic P- and S-wavefields, please refer to Wapenaar and Berkhout [1989] and Wapenaar and Haime [1990].

The iterative full wavefield modelling of the P- and S- wavefields is done in a similar way as described in chapter two of this thesis. However, the scattered P wavefield now comprise of the two-way full-elastic scattered P-waves i.e. $\delta\vec{P}_p^{+}$ and $\delta\vec{P}_p^{-}$, and the scattered S wavefield now comprise of two-way full-elastic scattered S-waves i.e. $\delta\vec{P}_s^{+}$ and $\delta\vec{P}_s^{-}$.

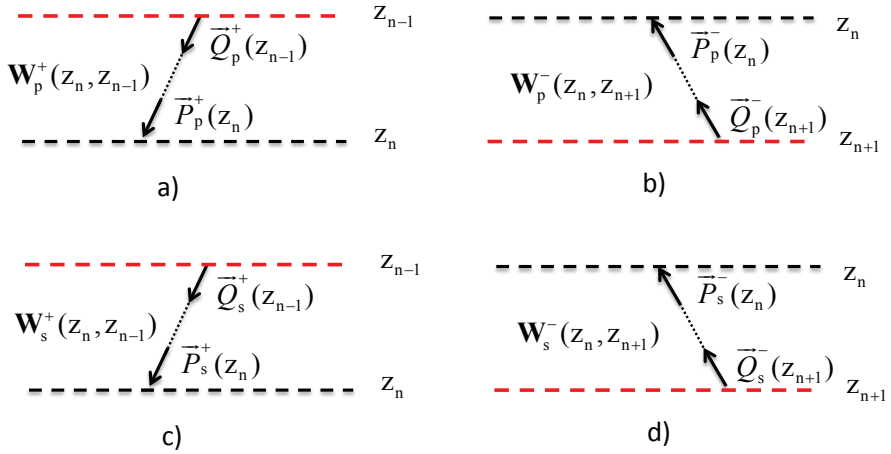

Figure 6.4: *Schematic diagram showing wavefield propagation between two depth levels for P- and S-wavefields. a) and c) show downward propagation of the downgoing P- and S-wavefields $\vec{Q}_p^+(z_{n-1})$ and $\vec{Q}_s^+(z_{n-1})$ from just below the depth level z_{n-1} to the downgoing P- and S-wavefield $\vec{P}_p^+(z_n)$ and $\vec{P}_s^+(z_n)$ just above the depth level z_n, using the propagation operator $\mathbf{W}_p^+(z_n, z_{n-1})$ and $\mathbf{W}_s^+(z_n, z_{n-1})$, respectively. Similarly, b) and d) show upward propagation of the upgoing P- and S-wavefield $\vec{Q}_p^-(z_{n+1})$ and $\vec{Q}_s^-(z_{n+1})$ from just above the depth level z_{n+1} to the upgoing P- and S-wavefield $\vec{P}_p^-(z_n)$ and $\vec{P}_s^-(z_n)$ just below the depth level z_n, using the propagation operator $\mathbf{W}_p^-(z_n, z_{n+1})$ and $\mathbf{W}_s^-(z_n, z_{n+1})$, respectively. $\mathbf{W}_p$ and $\mathbf{W}_s$ represents the propagation due to the P- and S-wave velocity, respectively.*

As described in chapter two of this thesis, the iterative full wavefield modelling includes iterative modelling of the total incident wavefield from above and from below. For elastic VSP data, we will define the modelling in the true source-receiver geometry, which is similar to modelling surface seismic wavefields, followed by selecting the upgoing and the downgoing wavefields at known receiver depths. In order to incorporate the converted wavefield in the modelling scheme, we have to model the incident downgoing P- and S- wavefields, i.e. $\vec{P}_p^+(z_n)$ and $\vec{P}_s^+(z_n)$, from above, and the incident P- and S- upgoing wavefields, i.e. $\vec{P}_p^-(z_n)$ and $\vec{P}_s^-(z_n)$, from below, respectively. We assume that for the time being that only P-sources are present at the surface z_0. For a given iteration i, the modelling equations can be written as:

$$\vec{P}_p^{+}(z_n)^{(i)} = \mathbf{W}_p^{+}(z_n, z_0)\vec{S}_p^{+}(z_0) + \sum_{m=0}^{n-1} \mathbf{W}_p^{+}(z_n, z_m)[\delta\vec{P}_p^{+}(z_m)]^{(i-1)}, \quad (6.2.14)$$

$$\vec{P}_p^{-}(z_n)^{(i)} = \sum_{m=n+1}^{N} \mathbf{W}_p^{-}(z_n, z_m)[\delta\vec{P}_p^{-}(z_m)]^{(i-1)}, \quad (6.2.15)$$

$$\vec{P}_s^{+}(z_n)^{(i)} = \sum_{m=0}^{n-1} \mathbf{W}_s^{+}(z_n, z_m)[\delta\vec{P}_s^{+}(z_m)]^{(i-1)}, \quad (6.2.16)$$

$$\vec{P}_s^{-}(z_n)^{(i)} = \sum_{m=n+1}^{N} \mathbf{W}_s^{-}(z_n, z_m)[\delta\vec{P}_s^{-}(z_m)]^{(i-1)}, \quad (6.2.17)$$

where $\vec{S}_p^{+}(z_0)$ represents the P-source wavefield at the surface. Note again that in the first step, $\vec{P}_p^{+}(z_n)^{(1)} = \mathbf{W}^{+}(z_n, z_0)\vec{S}_p^{+}(z_0)$, i.e. the direct source wavefield at all depth levels and other wavefields i.e. $\vec{P}_p^{-}(z_n)^{(1)}$, $\vec{P}_s^{+}(z_n)^{(1)}$ and $\vec{P}_s^{-}(z_n)^{(1)}$ are zero. Furthermore, as mentioned earlier, for walkaway VSP data modelling, we can select the upgoing and downgoing wavefields for all the spatial locations, i.e. both lateral and vertical location, where the receivers are present. The modelled VSP data is obtained by taking the sum of the upgoing and downgoing wavefields measured by the borehole receivers.

6.3 Elastic full wavefield modelling for a layered medium: numerical examples

In the previous section, we have discussed the mathematical formulation of the elastic full wavefield modelling. The iterative modelling of the incident P- and S-wavefields are a function of the two-way scattered P wavefield ($\delta\vec{P}_p^{+}$ and $\delta\vec{P}_p^{-}$) and the two-way scattered S wavefield ($\delta\vec{P}_s^{+}$ and $\delta\vec{P}_s^{-}$), which in turn are a function of the reflectivity and transmissivity matrices i.e. $\mathbf{R}_{pp}^{\cup}$, $\mathbf{R}_{ps}^{\cup}$, $\mathbf{R}_{pp}^{\cap}$, $\mathbf{R}_{ps}^{\cap}$, $\mathbf{R}_{sp}^{\cup}$, $\mathbf{R}_{ss}^{\cup}$, $\mathbf{R}_{sp}^{\cap}$, $\mathbf{R}_{ss}^{\cap}$, $\mathbf{T}_{pp}^{+}$, $\mathbf{T}_{ps}^{+}$, $\mathbf{T}_{pp}^{-}$, $\mathbf{T}_{ps}^{-}$, $\mathbf{T}_{sp}^{+}$, $\mathbf{T}_{ss}^{+}$, $\mathbf{T}_{sp}^{-}$ and $\mathbf{T}_{ss}^{-}$, given by Equation (6.2.9). Note that all these reflectivity matrices are angle-dependent, which shows complex behavior at critical and post-critical angles. Hence, the modelling as well as inversion of all these parameters together is not trivial. In order to simplify

$$\vec{R}_{pp}(s_x) = \frac{1}{2}(1-4\beta_0^2 s_x^2)\Delta\ln\rho + \frac{1}{2(1-\alpha_0^2 s_x^2)}\Delta\ln\alpha - 4\beta_0^2 s_x^2 \Delta\ln\beta, \quad (6.3.19)$$

$$\vec{R}_{sp}(s_x) = \frac{-s_x\alpha_0}{2\sqrt{1-\beta_0^2 s_x^2}}\left[\left(1-\beta_0^2 s_x^2 + 2\beta_0^2\frac{\sqrt{1-\alpha_0^2 s_x^2}\sqrt{1-\beta_0^2 s_x^2}}{\alpha_0\beta_0}\right)\Delta\ln\rho\right]$$
$$- \frac{-s_x\alpha_0}{2\sqrt{1-\beta_0^2 s_x^2}}\left[4\beta_0^2\left(s_x^2 - \frac{\sqrt{1-\alpha_0^2 s_x^2}\sqrt{1-\beta_0^2 s_x^2}}{\alpha_0\beta_0}\right)\Delta\ln\beta\right] \quad (6.3.20)$$

$$\vec{R}_{ss}(s_x) = -\frac{1}{2}(1-4\beta_0^2 s_x^2)\Delta\ln\rho - \left[\frac{1}{2(1-\beta_0^2 s_x^2)} - 4\beta_0^2 s_x^2\right]\Delta\ln\beta, \quad (6.3.21)$$

$$\vec{R}_{ps}(s_x) = \frac{\beta_0\sqrt{1-s_x^2\beta_0^2}}{\alpha_0\sqrt{1-s_x^2\alpha_0^2}}\vec{R}_{sp}(s_x). \quad (6.3.22)$$

Similarly, the angle-dependent transmissivity vectors of a grid point at an interface or discontinuity are given by (Aki and Richards [1980]):

$$\vec{T}_{pp}(s_x) = 1 - \frac{1}{2}\Delta\ln\rho + \left[\frac{1}{2(1-\alpha_0^2 s_x^2)} - 1\right]\Delta\ln\alpha, \quad (6.3.23)$$

$$\vec{T}_{sp}(s_x) = \frac{s_x\alpha_0}{2\sqrt{1-\beta_0^2 s_x^2}}\left[\left(1-\beta_0^2 s_x^2 - 2\beta_0^2\frac{\sqrt{1-\alpha_0^2 s_x^2}\sqrt{1-\beta_0^2 s_x^2}}{\alpha_0\beta_0}\right)\Delta\ln\rho\right]$$
$$- \frac{s_x\alpha_0}{2\sqrt{1-\beta_0^2 s_x^2}}\left[4\beta_0^2\left(s_x^2 + \frac{\sqrt{1-\alpha_0^2 s_x^2}\sqrt{1-\beta_0^2 s_x^2}}{\alpha_0\beta_0}\right)\Delta\ln\beta\right] \quad (6.3.24)$$

$$\vec{T}_{ss}(s_x) = 1 - \frac{1}{2}\Delta\ln\rho + \left[\frac{1}{2(1-\beta_0^2 s_x^2)} - 1\right]\Delta\ln\beta, \quad (6.3.25)$$

$$\vec{T}_{ps}(s_x) = -\frac{\beta_0\sqrt{1-s_x^2\beta_0^2}}{\alpha_0\sqrt{1-s_x^2\alpha_0^2}}\vec{T}_{sp}(s_x). \quad (6.3.26)$$

Here, α_0 and β_0 are the P-wave and S-wave background velocities. In the forward modelling, we assume that both the background P- and S-wave velocity models are known. Also in the forward modelling, we know the true logarithmic elastic contrast parameters. We can re-write the above four equations for $\vec{R}_{pp}$, $\vec{R}_{sp}$, $\vec{R}_{ss}$ and $\vec{R}_{sp}$ and the four equations for $\vec{T}_{pp}$, $\vec{T}_{sp}$, $\vec{T}_{ss}$ and $\vec{T}_{sp}$ in a simple way as a

function of elastic contrast parameters i.e. $\Delta \ln \rho$, $\Delta \ln \alpha$ and $\Delta \ln \beta$ as:

$$\vec{R}_{pp}(s_x) = a_{11}(s_x)\Delta \ln \rho + a_{12}(s_x) \ln \alpha + a_{13}(s_x) \ln \beta, \quad (6.3.27)$$

$$\vec{R}_{sp}(s_x) = a_{21}(s_x)\Delta \ln \rho + a_{22}(s_x) \ln \alpha + a_{23}(s_x) \ln \beta, \quad (6.3.28)$$

$$\vec{R}_{ps}(s_x) = a_{31}(s_x)\Delta \ln \rho + a_{32}(s_x) \ln \alpha + a_{33}(s_x) \ln \beta, \quad (6.3.29)$$

$$\vec{R}_{ss}(s_x) = a_{41}(s_x)\Delta \ln \rho + a_{42}(s_x) \ln \alpha + a_{43}(s_x) \ln \beta, \quad (6.3.30)$$

$$\vec{T}_{pp}(s_x) = 1 + b_{11}(s_x)\Delta \ln \rho + b_{12}(s_x) \ln \alpha + b_{13}(s_x) \ln \beta, \quad (6.3.31)$$

$$\vec{T}_{sp}(s_x) = b_{21}(s_x)\Delta \ln \rho + b_{22}(s_x) \ln \alpha + b_{23}(s_x) \ln \beta, \quad (6.3.32)$$

$$\vec{T}_{ps}(s_x) = b_{31}(s_x)\Delta \ln \rho + b_{32}(s_x) \ln \alpha + b_{33}(s_x) \ln \beta, \quad (6.3.33)$$

$$\vec{T}_{ss}(s_x) = 1 + b_{41}(s_x)\Delta \ln \rho + b_{42}(s_x) \ln \alpha + b_{43}(s_x) \ln \beta, \quad (6.3.34)$$

which can be written as a matrix equations as:

$$\begin{bmatrix} \vec{R}^{\cup}_{pp} \\ \vec{R}^{\cup}_{sp} \\ \vec{R}^{\cup}_{ps} \\ \vec{R}^{\cup}_{ss} \end{bmatrix} = \begin{bmatrix} a_{11} & a_{12} & a_{13} \\ a_{21} & a_{22} & a_{23} \\ a_{31} & a_{32} & a_{33} \\ a_{41} & a_{42} & a_{43} \end{bmatrix} \begin{bmatrix} \Delta \ln \rho \\ \Delta \ln \alpha \\ \Delta \ln \alpha \end{bmatrix} = \mathbf{A} \begin{bmatrix} \Delta \ln \rho \\ \Delta \ln \alpha \\ \Delta \ln \beta \end{bmatrix} \quad (6.3.35)$$

and

$$\begin{bmatrix} \overrightarrow{T}_{pp} \\ \overrightarrow{T}_{sp} \\ \overrightarrow{T}_{ps} \\ \overrightarrow{T}_{ss} \end{bmatrix} = \begin{bmatrix} 1 & b_{11} & b_{12} & b_{13} \\ 0 & b_{21} & b_{22} & b_{23} \\ 0 & b_{31} & b_{32} & b_{33} \\ 1 & b_{41} & b_{42} & b_{43} \end{bmatrix} \begin{bmatrix} 1 \\ \Delta \ln \rho \\ \Delta \ln \alpha \\ \Delta \ln \beta \end{bmatrix} \quad (6.3.36)$$

where the coefficients of matrices $\mathbf{A}$ and $\mathbf{B}$ are the functions of P-wave and S-wave background velocities, and ray-parameter s_x. Note that the superscripts '$\cup$' and '$+$' indicates that wavefield is traveling downwards before reflection and transmission, respectively. The computation of reflectivity and transmissivity for the wavefields traveling upwards are performed by flipping the model upside down, i.e. making a change in sign in the medium contrasts.

Given the true and background P-wave and S-wave velocities and the true density model in a forward problem, we can evaluate the angle-dependent reflectivity and transmissivity vectors as a function of ray-parameter s_x (from the approximations

Figure 6.11 illustrates an exact solution of the Zoeppritz equation, courtesy of CREWES Zoeppritz explorer 2.2, for the first reflector (as shown in Figure 6.6).

Specifically, Figure 6.11a, 6.11b, 6.11c and 6.11d show $\vec{R}_{pp}$, $\vec{R}_{sp}$, $\vec{R}_{ps}$ and $\vec{R}_{ss}$ respectively at one grid-point location for an interface separating two half spaces. The density, P-wave velocity and S-wave velocity for medium above the interface are $1000kg/m^3$, $2700m/s$ and $1500m/s$, respectively, and for the medium below the interface are $2000kg/m^3$, $3000m/s$ and $1700m/s$, respectively. Note that in all figures, the bold curve shows the real part and the dotted curve shows the imaginary part of the complex reflectivity at and above critical angle. Also, note the reflectivity becomes very complex at post-critical angles for incident S-waves i.e. for R_{ps} and R_{ss}. The dotted blue curve at +/- 30 degrees shows the cut-off point up to where the reflectivity value is used in the elastic forward modelling scheme. This corresponds to the reflectivity curves shown in Figures 6.9a, 6.9b, 6.9c and 6.9d. Figures 6.12 to 6.19 show an example of a common-shot gather modelled iteratively using the elastic full wavefield modelling scheme. Specifically, Figures 6.12, 6.14, 6.16 and 6.18 show an example common-shot gather for the P-wavefield modelled after the 1^{st}, 2^{nd}, 3^{rd} and 4^{th} iteration, respectively. Similarly, Figures 6.13, 6.15, 6.17 and 6.19 show an example common-shot gather for the S-wavefield modelled after the 1^{st}, 2^{nd}, 3^{rd} and 4^{th} iteration, respectively. Note that the dotted axis at depth $300m$, $550m$ and $780m$ annotated in all figures indicate the depth of the three reflectors used in the model. Also note that the surface multiples are not included in these modelling examples. As expected, in the elastic full wavefield modelling scheme, each iteration adds a higher order of scattered wavefields, i.e. a higher order of multiples for both P- and S-wavefields.

Furthermore, in the modelling scheme, the total upgoing wavefields at the surface represent the data equivalent to surface seismic data. Figures 6.20 shows an example of a common-shot gather for receivers located at the surface (i.e. surface seismic data) modelled after the 1^{st} and the 4^{th} iteration, showing the upgoing P-wavefield and the upgoing S wavefield.

We assume that the turning-waves incident on the borehole act as a nearly-horizontal wavefield that illuminates the salt-body beyond the borehole after which the receivers can record the reflections from the salt boundaries, as shown in Figure 7.1. Hence, we could formulate the forward modelling of the downgoing wavefield $\vec{P}^{+}(z'_n)$ and the upgoing wavefield $\vec{P}^{-}(z'_n)$ at any depth level z'_n in the orthogonal rotated coordinate system as:

$$\vec{P}^{+}(z'_n) \quad = \sum_{m=0}^{n-1} \mathbf{W}^{+}(z'_n, z'_m)[\delta\vec{P}(z'_m) + \vec{P_{inc}}(z'_0)], \tag{7.2.1}$$

$$\vec{P}^{-}(z_n) \quad = \sum_{m=n+1}^{N} \mathbf{W}^{-}(z'_n, z'_m)[\delta\vec{P}(z'_m)], \tag{7.2.2}$$

where $\mathbf{W}^{+}$ and $\mathbf{W}^{-}$ represent the downward and upward wavefield propagation operators, respectively, in the rotated coordinate system and $\vec{P}_{inc}(z'_0)$ represents the total wavefield coming from the source-side towards the borehole. Note that the vectors and matrices in the above formulation represent one frequency component of their respective wavefields or operators. The two-way scattered wavefield is given in terms of the reflectivity matrices as:

$$\delta\vec{P}(z'_n) = \mathbf{R}^{\cup}(z'_n)\vec{P}^{+}(z'_n) - \mathbf{R}^{\cap}(z'_n)\vec{P}^{-}(z'_n). \tag{7.2.3}$$

For small S-wave velocity contrasts and for pre-critical angles, $\mathbf{R}^{\cup}(z'_n) = -\mathbf{R}^{\cap}(z'_n)$, therefore, we can re-write the above equation for a two-way scattered wavefield as:

$$\delta\vec{P}(z'_n) = \mathbf{R}^{\cup}(z'_n)[\vec{P}^{+}(z'_n) - \vec{P}^{-}(z'_n)]. \tag{7.2.4}$$

Note that the incident wavefield $\vec{P}_{inc}(z'_0)$ on the receivers in the borehole is equivalent to the convolution of the source wavefield at the surface $\vec{S}(z_0)$ with the impulse response, $\mathbf{X}_s$ of the subsurface outside the target domain, at the source-side. Hence, the impulse response $\mathbf{X}_s$ accounts for all the scattering outside the target domain. If we have a blended source experiment (as discussed in chapter five), where the blended source is represented by $\vec{S_{bl}}(z_0)$, then the incident wavefield $\vec{P}_{inc,bl}$ can be written as:

$$\vec{P}_{inc,bl}(z'_0) = \mathbf{X}_s\vec{S}^{-}_{bl}(z_0) = \mathbf{X}_s\vec{S}(z_0)\vec{\Gamma}_{bl}(z_0), \tag{7.2.5}$$

where the blending operator $\vec{\Gamma}_{bl}(z_0)$ can be written as $\vec{\Gamma}_{bl}(z_0) = [\gamma_1, \gamma_2, \gamma_3, ..., \gamma_N]$, with $\gamma_n = a_n e^{-j\omega T_n}$ [see Berkhout, 2008]. In this case, T_n is a random time-shift applied to blend the sources and a_n is a scale factor. Note that $a_n = 0$ eliminate these sources in the blended experiment. We will use the term 'blending factor' to define the number of shots blended together in one experiment for which $a_n \neq 0$ [Soni and Verschuur, 2013b, 2014b].

To illustrate the illumination from the turning waves and reflections, we used a 1.5D sediment-flooded velocity model and a 2D density model with a vertical salt structure. The waves are simulated using a 2D acoustic finite-difference scheme for an offset source laterally located at $2700m$. Figure 7.2 shows the velocity and density models, and the simulated wavefield snapshots at different times with reference to the source excitation time at $t = 0s$. Note that the turning wavefront illuminating the vertical salt-boundary generates primaries and multiples upon reflection. In this example, we have assume a rigid sea-air boundary at z_0 (i.e. without surface-multiples). A vertical borehole laterally located at $1000m$, close to the salt structure will record the primary and multiple-reflected turning waves. Hence, the measurements can be used to image the salt boundary.

We have discussed the forward model for the turning waves which laterally illuminate the steeply-dipping salt structures in the target domain. We have also defined the modelling equations for both unblended and blended VSP experiments. Hence, in the rotated coordinate system, we can also write the full wavefield migration as an optimization scheme to minimize the following objective function:

$$J = \sum_{s} \sum_{\omega} ||\vec{P}^{-}(z_0') - \vec{P}^{-}_{est}(z_0')||_2^2, \tag{7.2.6}$$

where $\vec{P}^{-}(z_0')$ and $\vec{P}^{-}_{est}(z_0')$ are the observed and estimated data at the borehole in the rotated coordinate system, for unblended or blended VSP experiments, summed over all frequencies and for all source experiments. The objective function is minimized using an iterative conjugate gradient scheme to estimate the subsurface reflectivity (as described in chapter three).

Note that the estimated data at the receivers are computed using Equation (7.2.2) for an upgoing wavefield at depth level z_0', in the rotated coordinate system. In the migration, we have a smooth migration velocity model for the target domain. However, we do not require the velocity model for the domain outside the target. For the incident source-wavefield, we can use the direct arrival recorded at the borehole receivers. In case of scatters in the domain outside the target, we expect to get some crosstalk in the image, however, the inversion-based imaging process iteratively suppresses the noise, providing a reasonable image. For real situations, we do require some knowledge of the subsurface sediment-flood velocity, in order to design the VSP acquisition geometry. We do not discuss the acquisition design methodology to acquire turning waves in this paper.

For illustration, we perform FWM to image the data measured using the configuration shown in Figure 7.2. Figure 7.3 illustrates the image obtained after the 10^{th} iteration of FWM for the target domain.

We performed the full wavefield migration on the VSP data simulated using both the density models (shown in Figure 7.4 a and 7.4b) to estimate the P-P image of the target domain in the rotated coordinate system (as explained earlier). The imaging was performed for unblended and blended data. Note that we have numerically blended the measured data to illustrate imaging of the blended VSP data [for more details on blended VSP imaging, see Soni and Verschuur, 2013b, 2014a]. We illustrate the imaging for blending factors one (unblended) and four in this chapter.

Figure 7.11 show the images obtained after the 1^{st} and the 10^{th} iteration of FWM. Specifically, Figures 7.11a and 7.11e show the images for VSP data simulated with the density model without a near-surface scatterer (Figure 7.4a) for blending factors one and four, respectively, after the 1^{st} iteration. The corresponding images after the 10^{th} iteration are shown in Figures 7.11b and 7.11f. Similarly, Figures 7.11c and 7.11g show the images for VSP data simulated with the density model with a near-surface scatterer (Figure 7.4b) for blending factors one and four, respectively, after the 1^{st} iteration. Again, the corresponding images after the 10^{th} iteration are shown by Figures 7.11d and 7.11h.

Note that the images after the 1^{st} iteration are equivalent to results from conventional imaging techniques using the primary-reflections only. The inversion-based FWM helps to improve the amplitude of the steeply-dipping or overturned salt flank, using the full-wavefield. Furthermore, we illustrate imaging of the blended VSP experiment, where FWM also helps to suppress the crosstalk noise in the image due to wavefield interference as expected and yields a reasonable image [Verschuur and Berkhout, 2011; Soni and Verschuur, 2014b]. Finally, we illustrate the effect of a near-surface high-contrast scatterer in the imaging, where the total illuminating wavefield enhances due to the coda. The FWM also effectively handles the crosstalk due the scattering in the illumination wavefield that occurs outside the target domain.

7.4 Discussion

Walkaway VSP data has proven to be useful in imaging steeply dipping or overturned salt-flanks. We have discussed an extended FWM approach using horizontal wavefield extrapolation to incorporate turning waves in VSP data to image steep structures. In this chapter, we assume that we know the total incident wavefield at the borehole that illuminates the target domain. In practice, since VSP measurements are multicomponent, we can perform directional decomposition of the wavefield to estimate incident wavefield and reflected wavefield from the total observed data. Furthermore, we have illustrated that FWM can handle both unblended and blended VSP data effectively for imaging salt-flanks. The inversion-based imaging helps to suppress the crosstalk due to a blended experi-

8

Field data application: deep-water Gulf of Mexico data

8.1 Introduction

In this chapter, we will illustrate the application of full wavefield migration on a field data set from deep-water in the Gulf of Mexico. The dataset comprises of two nearly orthogonal walkaway VSP lines. The following sections will discuss the VSP acquisition geometry, preprocessing used before FWM and finally the imaging results.

8.2 VSP geometry and preprocessing

The walkaway VSP data used to illustrate FWM were acquired in deep-water of the Gulf of Mexico in a block under Anadarko Petroleum Corporation. The water-bottom depth in this area is approximately $1200m$. We have received the PP reflection data after basic preprocessing. The data comprises of two nearly orthogonal walkaway VSP lines and a set of nine receivers in a deep borehole. The source separation on the surface is approximately $60m$, with the maximum source offset from the wellhead around $3000m$. The receivers were located from $3230m$ to $3350m$, with an inter-geophone spacing of $15m$. For a detailed description of this data, please see O'Brien et al. [2013a,b]. These papers discuss imaging of first-order free-surface multiples using the mirror-model concept. Figure 8.1 illustrates the map view of the two VSP lines. Furthermore, Figures 8.2 and 8.3 show all nine received pre-processed common-receiver gathers for line A and line

9

Conclusions, recommendations and future research

In this chapter, we will discuss the conclusions and recommendations based on this research and future research plans. Finally, we will discuss an overview of various seismic inversion schemes.

9.1 Conclusions

In seismic imaging, multiples in the measured data are generally considered as noise. If they are not removed prior to a conventional primaries-only migration schemes, they create artifacts i.e. false structures in the image that can make the interpretation deceptive. However, the multiples provide an extra source of illumination in the area where the primary wavefield may have failed to illuminate the field. In this research, we have introduced an imaging technology termed full wavefield migration, which aims to utilize the multiples (both surface multiples and internal multiples) in the observed data in imaging. This technology can handle both surface and borehole seismic data. In this research we discuss its application on borehole seismic or vertical seismic profiling (VSP) data. The primary-only images of VSP data suffer from imaging artifacts and low illumination as we move further away from the well. Hence, using multiples in the imaging has proven to improve illumination and resolution significantly in VSP images.

In chapter two, three and four, we have discussed the forward modelling, the inversion scheme and illustrated various synthetic examples, respectively. The

numerical examples illustrates the advantages of using the full wavefield in the imaging of VSP data in terms of better illumination and improved resolution of VSP images. The multiples help to image in the overburden area above the receivers where the primaries-only wavefields fail to illuminate. The closed-loop or inversion-based imaging scheme helps us to get a true-amplitude image that can explain the full wavefield in the measured data. Furthermore, the inversion scheme depends on an accurate estimation of the source wavefield. In VSP data, it is relatively easier compared to surface seismic data to estimate the source wavefield from the direct arrivals in the measured data.

In chapter five, we have illustrated the potential of FWM to image blended source VSP data, without the need of a separate active deblending step. Again, the inversion-based imaging process can handle complex source wavefields more effectively than a cross-correlation based imaging scheme. The estimated reflectivity image explains the full wavefield of the measured blended VSP data.

In chapter six, we introduced the extension of acoustic full wavefield migration to incorporate converted waves, i.e. elastic full wavefield migration. We have shown elastic full wavefield modelling using a horizontally layered model and the angle-dependent elastic reflectivity parameters derived from Aki and Richards approximation of the Zoeppritz equations. Understanding the elastic full wavefield modelling is critical to begin the inversion scheme. The inversion of elastic or multi-component VSP data is discussed as one of the future research plans.

In chapter seven, we have extended FWM by incorporating the turning waves using horizontal or orthogonal wavefield extrapolation schemes in a rotated coordinate system. We demonstrate its use in imaging near-vertical or steeply-dipping salt flanks.

In chapter eight, we have illustrated the application of the proposed imaging scheme on two sets of walkaway VSP data from a deep-water region in the Gulf of Mexico. Only one set of receiver array was placed very deep and close to the reservoir to record the data. We have shown that the image obtained from full-wavefield migration has a wider illumination especially in the shallow region due to strong surface multiples present in the data. However, the image could have been better in terms of illumination at the reservoir level if the acquired data had two or three sets of receivers recorded at different depths both in the overburden and close to the reservoir. The proposed ideal geometry of the VSP data to make better use of full-wavefield migration must have receiver data at different depth levels. This aspect is discussed in the next section.

In terms of an overall conclusion from this research work - we have shown the feasibility and applicability of full wavefield migration in imaging VSP data. We have demonstrated that multiples, when handled properly, can add extra illumination, especially away from the well vicinity. However, in the current scheme, we have mostly restricted ourselves to estimate an angle-independent P-P reflec-

tivity of the subsurface. VSP data are often multicomponent records. Hence, ideally we need to estimate the elastic angle-dependent reflectivity to explain the multicomponent measurements. Also, the current imaging scheme assumes isotropic medium properties, whereas there are various geological scenarios where the anisotropic behavior of P and S-wave velocities are pronounced. Furthermore, from the field data experiment, we found that the acquisition geometry is crucial to make FWM more effective in terms of illumination in the deep as well as suppressing remnant crosstalk. A walkaway VSP data with multi-level receiver arrays placed at different depth levels can help to improve illumination especially at the deep reservoir level. Finally, like any migration technology, we require a smooth background velocity model.

In the next section, based on this research, we would like to discuss some recommendations and future research plans to image VSP data using FWM.

9.2 Recommendations and future research plans

Angle-dependent elastic imaging of VSP data

In this thesis, we pre-dominantly focused on structural imaging of VSP data in an acoustical sense (considering only PP reflections). However, in reality, the earth layers have angle-dependent reflection properties that cause wave mode conversion. A simplified elastic full wavefield modelling scheme is discussed in chapter six. Our future research plan includes incorporating the converted waves in the measured multi-component VSP data to estimate the full elastic reflectivity parameters i.e. $\mathbf{R}_{pp}$, $\mathbf{R}_{ps}$, $\mathbf{R}_{sp}$ and $\mathbf{R}_{ss}$. Figure 9.1 shows a block diagram for such a scheme.

One of the major challenges towards elastic imaging would be proper parametrization of the reflection coefficients, especially for high-contrast media where the angle-dependent reflection coefficients become complex-valued at and above post-critical angles.

Extension to anisotropic velocities

In this thesis, we have assumed an isotropic medium for imaging. As a future extension to FWM on VSP and surface data, anisotropic full wavefield migration is an ongoing research topic [for some introductory examples, see Alshuhail et al., 2014].

Extension to 3D VSP data and simultaneous VSP-surface data imaging

One of the future research plans is to perform 3D full wavefield migration on 3D VSP data. The concepts discussed in this thesis are illustrated for 2D walkaway VSP data. However, the concepts of FWM are equally applicable in 3D and can be extended to handle 3D VSP geometries. Furthermore, handling surface

Now we have used three sets of 11 receivers, with depth spacing of $10m$ each, at depth levels starting from $1250m$, $1550m$, and $1950m$. Figure 9.2 shows the images obtained using the three receiver sets separately as well as all together, for both primaries-only wavefields and the full-wavefield. Note that the crosstalk that appeared at different depth levels due to the limited number of receivers at one depth level eventually got suppressed when the simultaneous imaging is done for all three sets. Hence, using multi-level receivers helps better convergence of the algorithm.

Joint migration-inversion of VSP data

In this thesis, we have assumed that for the imaging of VSP data using full wavefield migration, we have a proper migration velocity model derived from surface seismic data or well logs. However, this might not be true in all cases. Furthermore, in chapter four, we illustrated that if we use a wrong velocity model in full wavefield migration, the data-misfit in the inversion scheme is considerably higher. This residual could also be used to drive the update of the velocity model. The scheme to update or estimate both the reflectivity image and the migration velocity model is termed joint-migration inversion (JMI) [for an introduction to JMI and applications in surface seismic data, see Berkhout, 2012; Staal and Verschuur, 2012, 2013; Staal et al., 2014]. We propose that joint-migration inversion can be equally important for borehole seismic or VSP data. Figure 9.3 shows a block diagram for the inversion scheme in JMI.

As a preliminary test, we will demonstrate an example of JMI for VSP data. Figure 9.4 shows the true velocity model, the initial velocity model and the update velocity model using JMI. The imaging results are depicted in Figure 9.5. Figure 9.6 shows the same images overlaid with the true reflectivity curves. Note that the FWM image using the updated velocity model, as shown in Figure 9.5d, is improved in terms of imaging quality as well as the depth of the reflectors. However, in this preliminary test, we found that the strong transmitted direct arrivals are too dominant in the inversion schemes. We recommend that in future research, we need to test different weighting for the reflection and transmitted data to make better use of both components.

Incorporating multiples in 3D VSP acquisition-design

In today's industrial practice, 3D VSP acquisition design involves generating synthetic data using a finite-difference scheme for various possible geometry designs and performing conventional imaging using the simulated data. A prior 3D velocity model derived using surface seismic or well-logs are used in the finite-difference schemes. Illumination by primary wavefields are also studied using 3D ray-tracing tools to understand the impact of different geometries. The acquisition geometry that yields the best image is selected.

However, these huge 3D VSP acquisitions can be optimized by including strong

attenuating media [for example see Kjartansson, 1979; Johnston and Toksoz, 1980; Krebes and Hron, 1980; Bourbiè and Serrano, 1983; Varela et al., 1993; Liao and McMechan, 1996]; and on the subject of inverse Q-filtering and estimation of Q-factor using both surface seismic and VSP data [for example see Hargreaves and Calvert, 1991; Wang, 2002; Guerra and Leaney, 2006; Wang, 2006, 2008; Blias, 2012; Wang, 2014]. The details of various algorithm on Q estimation is beyond the scope of this thesis, however, we will discuss briefly a possible way to incorporate absorption in FWM and JMI by including the effects in the wavefield extrapolation.

Basically, if we see in 1D case using the phase shift operator concept [Gazdag, 1978], we can define the wavefield extrapolation between two depth levels separated by Δz as [Varela et al., 1993; Wang, 2008]:

$$P(z + \Delta z, \omega) = P(z, \omega) e^{jk_z \Delta z}, \tag{9.2.2}$$

where P is the Fourier transform of the wavefield, z is the depth location where wavefield is measured, ω is the angular frequency and k_z is the wavenumber in z-direction. Note again that forward or inverse extrapolation implies taking Δz as negative or positive, respectively. Now, to include absorption in the above equation, k_z is modified and become a complex function of frequency, given by:

$$k_z = -\left(\frac{\omega}{V} + j\alpha\right), \tag{9.2.3}$$

where V is the frequency-dependent phase velocity[2] and α is the absorption coefficient. Generally, α is a function of frequency which represents the dissipative attenuation and given by $\alpha = \omega/2QV$. Quality factor Q is assumed to be constant within the seismic bandwidth. Further, the phase velocity is also a function of frequency that accounts for dissipative dispersion in the model. Note that there are several discussions on the form of frequency dependence on the phase velocity, see for example Kolsky [1956]; Futterman [1962]; Robinson [1979]; Kjartansson [1979]. Also, Toverud and Ursin [2005] discuss various attenuation models using VSP data comprehensively. The resulting expression, which is valid for relatively large and constant Q is given by:

$$\frac{V}{V_r} \simeq 1 - \frac{1}{\pi Q} \ln\left(\frac{\omega}{\omega_r}\right), \tag{9.2.4}$$

where ω_r is the reference angular frequency, V_r is the propagation velocity in the reference frequency, which is given by the ratio of the distance traveled and its time equivalent, $\Delta\tau$, i.e. $V_r = \Delta z/\Delta\tau$. In other words, $\Delta\tau$ is the incremental traveltime at the reference frequency ω_r. Substituting Equations (9.2.3) and

[2]Phase velocity: The velocity of any given phase (such as a trough) or a wave of single frequency; it may differ from group velocity because of dispersion. Sometimes called ŚtroughŠ velocity or ŚpeakŠ velocity [Sherrif, 2002].

(9.2.4) in (9.2.2), and changing depth to its equivalent in time, we get:

$$P(\tau + \Delta\tau, \omega) = P(\tau, \omega)U(\Delta\tau, \omega)e^{-j\omega\Delta\tau}, \tag{9.2.5}$$

where $U(\Delta\tau, \omega)$ is the absorption operator given by:

$$U(\Delta\tau, \omega) = \exp\left(\frac{\omega\Delta\tau}{Q}\left[0.5 + \frac{j}{\pi}\ln\left(\frac{\omega}{\omega_r}\right)\right]\right). \tag{9.2.6}$$

From Equation (9.2.5), we can clearly see that the propagation of the wavefield from one depth level to the next include two separate terms, one accounting for the phase shift (or time shift)and other being the absorption operator U.

A similar approach in the propagation operator can be used for incorporating FWM in attenuating media, if Q-factor is known. For unknown Q-factor, future research can include simultaneous estimation of reflectivity and a complex velocity model in JMI, where the imaginary term in the velocity model accounts for the absorption in the observed data. In slightly different approaches, we have also seen estimation of Q-factor in recent research where they are estimated in ray-based tomography [for example, see Cavalca et al., 2011] and full waveform inversion [for example, see Bai and Yingst, 2013].

9.3 Seismic inversion: an overview of various schemes

In this section, we discuss the similarities and differences in the concept of full wavefield migration (FWM) and joint migration-inversion (JMI), full waveform inversion (FWI) for velocity estimation, simultaneous impedance - background model inversion in FWI, least-squares reverse time migration (LSQRTM), velocity perturbation and impedance perturbation inversion using modified RTM and contrast-source inversion (CSI). Note that all of these inversion-based processes aimed to estimate a set of parameters from the measured seismic data. The main difference in all these schemes lies in the model parametrization, the forward modelling operator used in the inversion as well as the underlying assumption on the type of data (primary-only, full wavefield, diving waves, etc). In this discussion, we will present an overview of various schemes, and exclude the comparison of their computational costs involved. Figure 9.8 list these inversion schemes in a chart diagram, highlighting the output parameters in them.

In JMI, the parameters to estimate are reflectivity and background (migration) velocity. We assume a scale separation between these two parameters, i.e. reflectivity accounts for the amplitude behavior and background velocity accounts for phase changes (wavefield propagation) in the seismic measurements. In FWM, we assume that a background velocity is known and, therefore, we aim to estimate only the subsurface reflectivity. In JMI and FWM, the forward modelling operator iteratively builds all the scattering in the wavefield and corrects for transmission effects. Hence, the inversion process uses all the orders of scattering to estimate the subsurface parameters. Note that the scale separation also helps to make the JMI process robust in terms of initial velocity model and it does not suffer from cycle skipping[3] issues [for a discussion, please see Staal et al., 2014]. For an extensive discussion on FWM and JMI, see also Berkhout [2012, 2014a,b,c]. Further, the estimated reflectivity could include the angle-dependent behavior of the main interfaces that in turn can be used for AVO-type inversion or detailed reservoir studies. Also note that the forward iterative equation used in FWM complies with the Generalized Bremmer series (See Appendix A for a discussion on this).

In FWI, the parameters to estimate are the high-resolution elastic properties of the subsurface i.e. P-wave velocity, S-wave velocity and density. In most cases, the forward modelling operator used in FWI is a finite-difference operator, therefore there is no scale-separation between the amplitude and propagation behavior of the wavefield. This make the inversion scheme highly non-linear with respect to model parameters and often suffers from cycle skipping. Therefore, the success of the scheme is highly dependent on the availability of very low frequencies in the data as well as the starting model. For an extensive discussion on FWI, see Lailly [1983]; Tarantola [1986, 1987]; Virieux and Operto [2009]; Warner et al. [2013]. Recent advancement in broadband acquisition is proving to play a major role in improving the FWI results [ten Kroode et al., 2013]. Also note that most of the recent practical applications are restricted to use only diving waves in the measured data. Also, the final product - a high-resolution velocity model is not yet appreciated in the current practice, because the obtained model are in turn smoothed and used in the conventional migration algorithms to obtain subsurface images. The latter usually do not account for multiples in the data.

In the same family of FWI, we also saw proposals to estimate simultaneously the background model and impedances (both P-wave impedance and S-wave impedance). This is another way to do scale separation, where the forward modelling operator is based on the impedance and background model. For introductory discussions on this type of inversion, see Snieder et al. [1989]; Cao et al. [1990]. Let us compare this inversion scheme with JMI in terms of parameterization. We know that reflectivities are the boundary properties of the subsurface.

[3]Cycle skipping: jumping a leg in correlating events, as may occur in matching non corresponding peaks in automatic statics programs. [Sherrif, 2002]

They are physically equivalent to the impedance contrasts or directional gradient of impedance, but not impedance itself. Unlike impedance (acoustic or elastic), it includes the angle-dependent reflection behavior at an interface. On the other hand, impedance are the layer properties without any angle-dependent information. Further, the earlier development of this type of inversion scheme assumes Born-approximation i.e. accounting only for primary wavefields in the data, to obtain a smooth background model. This inherently assumes that higher order of scattering is removed from the measured data.

Reverse time migration (RTM) [Baysal et al., 1983; McMechan, 1983] aim to estimate subsurface reflectivity with an underlying linear single-scattering assumption. The least-squares RTM makes the scheme closed-loop, where the reflectivity or the structural image can be updated iteratively using only primary wavefields [Yao and Jakubowicz, 2012a,b; Dai et al., 2012; Zheng and Schuster, 2014; Zhang et al., 2014a; Tan and Huang, 2014]. A modified version of RTM has been proposed recently Zhang et al. [2014b], which aim to estimate subsurface impedance perturbation and velocity perturbation using the primary-only wavefield. In this scheme, the output angle-gathers using a modified imaging condition allows to estimate the impedance perturbation from the near-angle stacked image and the velocity perturbation from the far-angle image. This scheme makes a good intermediate link between imaging using RTM to FWI. In this modified RTM scheme, the velocity perturbation can provide high-resolution details, although it is limited, of course by the small-angle approximation.

Further, we also saw proposals to extend the concept of RTM (generally termed as nonlinear RTM) to incorporate multiples and also converted wavefields through modifying the imaging condition. Non-linear or multiple least-squares reverse time migration (NLSQRTM) extends the parameter estimation by including the interaction of multiples through modifying the imaging condition, modifying wavefield extrapolation and aim to estimate a scattering contrast model [Fleury, 2013] in an acoustic scenario. However, this inversion scheme does not give an integrated subsurface reflectivity as an output. Instead of one output, it gives four sub-images that represent same subsurface from different aspects. The non-linear imaging condition is further extended in elastic case and discussed comprehensively in Ravasi and Curtis [2013]. The modified nonlinear imaging condition accounts for multiply scattered and multiply converted waves.

Finally, Contrast Source inversion (CSI) [van den Berg and Kleinman, 1997; van den Berg et al., 1999; Abubakar et al., 2008; Haffinger et al., 2013; Rizzuti and Gisolf, 2014a,b] aim to estimate the high-resolution elastic contrast parameters from seismic measurements. The method iteratively solves the forward scattering equation through simultaneous update of contrast-sources (i.e. the perturbed wavefields) and the actual medium contrast for a known reference medium. It uses the full wavefield by iteratively adding higher order of scattering with each iteration. The contrast parameters (χ) for an elastic case include $\chi_\kappa = (\kappa - \kappa_b)/\kappa_b$,

$\chi_M = (M - M_b)/M_b$ and $\chi_\rho = (\rho - \rho_b)/\rho_b$, where κ is the compressibility, M is the shear compliance and ρ is the density [Rizzuti and Gisolf, 2014b].

Based on the overview of various inversion schemes as discussed above, we can say that for the future research, we will see efforts to develop an inversion-scheme that will help to obtain the best possible structural image as well as true-amplitude angle-dependent image gathers, using the full-wavefield. Additionally, it should also aim to estimate the redatumed wavefields (full-wavefield redatuming) above the reservoir level (or depth of interest), with all the overburden effects removed, for a high-resolution reservoir-oriented elastic inversion.

A

Derivation of iterative full wavefield modelling using the seismic representation theorem

A.1 Introduction: two-way and one-way wave equations

This appendix is inspired by the lectures on 'Advanced wave theory for geoscientists, taught by professor Kees Wapenaar and professor Jacob Fokkema during February-March 2014 at CiTG, Delft University of Technology, The Netherlands. Here, we are going to derive the iterative full wavefield modelling scheme using the well-known Seismic Representation theorem [Fokkema and van den Berg, 1993]. In this appendix, we will use the lecture notes from the course, the details of which can be found in Wapenaar and Berkhout [1989], Wapenaar and Grimbergen [1996]; Wapenaar [1996a] and Wapenaar [1996b].

We aim to relate the one-way representation of seismic data to arrive at the Generalized Bremmer series which is an iterative scheme for computing upgoing and downgoing wavefield and then relate it to the concept of full wavefield modelling (discussed in chapter two). Note that in this appendix, the discussion is restricted to the acoustic case, however, using the same principles, the derivation can be extended to elastic wavefields case. Further, we will derive the equations in wavenumber-frequency domain (for an laterally invariant medium), however the derivation can be easily generalized in space-frequency domain (incorporating laterally heterogeneous medium). Let us start by defining the two-way wave equation.

We assume a laterally invariant medium as shown in Figure A.1, with z the direction of wavefield propagation. Begin figure End figure For a laterally homogeneous

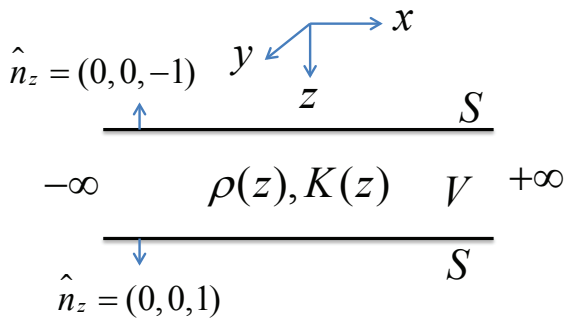

Figure A.1: *Schematic diagram showing the coordinate system and laterally invariant medium, bounded by surfaces S and contain volume V.*

medium, the linearized equation of continuity and motion in the wavenumber-frequency domain can be written as:

$$-jk_xV_x - jk_yV_y + \frac{\partial V_z}{\partial z} + \frac{j\omega}{K}P = j\omega I_v, \tag{A.1.1}$$

where V_x, V_y and V_z represents velocity vector components in x, y, and z direction, respectively; I_v represents the volume density of volume injection and P represents the acoustic pressure. Note that V_x, V_y, V_z, I_v and P are all functions of k_x, k_y, z and ω. They are not used in the equation above for brevity. Similarly, the linearized equation of motion can be written as:

$$\begin{bmatrix} -jk_xP \\ -jk_yP \\ \frac{\partial P}{\partial z} \end{bmatrix} + j\omega\rho \begin{bmatrix} V_x \\ V_y \\ V_z \end{bmatrix} = \begin{bmatrix} F_x \\ F_y \\ F_z \end{bmatrix}, \tag{A.1.2}$$

where F_x, F_y and F_z are the vector components in x, y and z for volume density of the external force, respectively. Note again that F_x, F_y and F_z are all functions of k_x, k_y, z and ω. Also, $\rho = \rho(z)$ and $K = K(z)$ represents the density and the compression modulus, respectively. Now eliminating V_x, V_y and V_z from Equations (A.1.1) and (A.1.2) (for detail derivation, see [Wapenaar and Berkhout, 1989]), we get:

$$\rho\frac{\partial}{\partial z}\left(\frac{1}{\rho}\frac{\partial P}{\partial z}\right) + (k^2 - k_x^2 - k_y^2)P = -D, \tag{A.1.3}$$

where $D = D(k_x, k_y, z, \omega)$ represents the source term given by:

$$D = -\omega^2 \rho I_v + jk_x F_x + jk_y F_y - \rho \frac{\partial}{\partial z}\left(\frac{1}{\rho} F_z\right). \tag{A.1.4}$$

Note that $k^2 = \frac{\omega^2}{c^2(z)}$ and $c(z) = \sqrt{\frac{K(z)}{\rho(z)}}$.

Now, eliminating the V_x and V_y related terms for laterally invariant medium, we can represent the two-way wave equation in a compact operator notation as [Wapenaar and Berkhout, 1989]:

$$\partial_z \mathbf{Q} - \mathbf{A}\mathbf{Q} = \mathbf{D}. \tag{A.1.5}$$

Note again that in above equation, $\mathbf{Q} = \mathbf{Q}(k_x, k_y, z, \omega)$, $\mathbf{A} = \mathbf{A}(k_x, k_y, z, \omega)$ and $\mathbf{D} = \mathbf{D}(k_x, k_y, z, \omega)$. For brevity, the terms between brackets is not explicitly written. Furthermore, in the aforementioned equation, $\mathbf{Q}$ is the two-way wavefield matrix defined as:

$$\mathbf{Q} = \begin{bmatrix} P \\ V_z \end{bmatrix}, \tag{A.1.6}$$

$\mathbf{D}$ is the two-way source matrix defined as:

$$\mathbf{D} = \begin{bmatrix} F_z \\ \frac{1}{j\omega\rho}\left(-\omega^2 \rho I_v + jk_x F_x + jk_y F_y\right) \end{bmatrix}, \tag{A.1.7}$$

and the two-way operator $\mathbf{A}$ connecting the wavefields and sources is defined as:

$$\mathbf{A} = \begin{bmatrix} 0 & -j\omega\rho(z) \\ \frac{k_z^2(z)}{j\omega\rho(z)} & 0 \end{bmatrix}. \tag{A.1.8}$$

Note that $k_z^2(z) = k^2(z) - k_x^2 - k_y^2$. Further, the two-way operator $\mathbf{A}$ can be decomposed using eigenvalue decomposition, and can be written as:

$$\mathbf{A} = \mathbf{L}\mathbf{\Lambda}\mathbf{L}^{-1} = \begin{bmatrix} 1 & 1 \\ \frac{k_z}{\omega\rho} & \frac{-k_z}{\omega\rho} \end{bmatrix} \begin{bmatrix} -jk_z & 0 \\ 0 & jk_z \end{bmatrix} \frac{1}{2} \begin{bmatrix} 1 & \frac{\omega\rho}{k_z} \\ 1 & \frac{-\omega\rho}{k_z} \end{bmatrix} \tag{A.1.9}$$

Note that $k_z = \sqrt{(k_2 - k_x^2 - k_y^2)}$ when $k_x^2 + k_y^2 \leq k_2$ and $k_z = -j\sqrt{(k_x^2 k_y^2 - k_2)}$ when $k_x^2 + k_y^2 > k_2$.

Now, let us discuss the one-way wave equation. We define the one-way wave vector $\mathbf{P}$ and the one-way source vector $\mathbf{S}$, respectively, as:

$$\mathbf{P} = \begin{bmatrix} P^+ \\ P^- \end{bmatrix}, \mathbf{S} = \begin{bmatrix} S^+ \\ S^- \end{bmatrix}, \tag{A.1.10}$$

where P^+ and P^- represent the downgoing and the upgoing pressure waves and S^+ and S^- represent the downgoing and the upgoing source wavefield.

Further, the one-way and two-way wave vectors are related as [Ursin, 1983]:

$$\begin{aligned} \mathbf{Q} &= \mathbf{L}\mathbf{P} \\ \mathbf{D} &= \mathbf{L}\mathbf{S} \end{aligned} \tag{A.1.11}$$

Substituting Equations (A.1) and (A.1) in (B.1.7) and solving systematically, we get the one-way wave equation from the two-way wave equation:

$$\begin{aligned} &\partial_z \mathbf{Q} - \mathbf{A}\mathbf{Q} = \mathbf{D} \\ &\Leftrightarrow \partial_z(\mathbf{L}\mathbf{P}) - \mathbf{L}\mathbf{\Lambda}\mathbf{P} = \mathbf{L}\mathbf{S} \\ &\Leftrightarrow \mathbf{L}^{-1}\partial_z(\mathbf{L}\mathbf{P}) - \mathbf{\Lambda}\mathbf{P} = \mathbf{S} \\ &\Leftrightarrow \partial_z \mathbf{P} - \{\mathbf{\Lambda} - \mathbf{L}^{-1}\partial_z \mathbf{L}\}\mathbf{P} = \mathbf{S} \\ &\Leftrightarrow \partial_z \mathbf{P} - \mathbf{B}\mathbf{P} = \mathbf{S} \end{aligned} \tag{A.1.12}$$

Here, operator $\mathbf{B} = \mathbf{\Lambda} - \mathbf{L}^{-1}\partial_z \mathbf{L}$ connects the one-way wavefield matrix $\mathbf{P}$ to the one-way source matrix $\mathbf{S}$. Note that $\mathbf{\Lambda}$ governs the one-way wavefield propagation and matrix $\mathbf{\Theta} = -\mathbf{L}^{-1}\partial_z \mathbf{L}$ governs the scattering due to vertical variation in the medium parameters. The matrix $\mathbf{\Lambda}$ is a function of medium slowness (as given in Equation (A.1)) and $\mathbf{\Theta}$ is a function of reflection and transmission coefficients written as:

$$\mathbf{\Theta} = \begin{bmatrix} T^+ & R^\cap \\ -R^\cup & -T^- \end{bmatrix} = \begin{bmatrix} 1 + R^\cup & -R^\cup \\ -R^\cup & -(1 - R^\cup) \end{bmatrix}, \tag{A.1.13}$$

where $R^\cup$ and $R^\cap$ represent the downgoing and upgoing reflection coefficients, and as mentioned in chapter two, $R^\cup = -R^\cap$ in the acoustic approximation. T^+ and T^- represent the downgoing and upgoing transmission coefficients and from the continuity relationship, we have $T^+ = 1 + R^\cup$. The relationship between the propagation term Λ and propagation operator matrices $\mathbf{W}$ (as introduced in chapter two) can be written as:

$$\mathbf{W}(z + \Delta z, z) = \exp(\Lambda \Delta z) = \begin{bmatrix} e^{-jk_z \Delta z} & 0 \\ 0 & e^{jk_z \Delta z} \end{bmatrix} = \begin{bmatrix} \mathbf{W}^+ & 0 \\ 0 & \mathbf{W}^- \end{bmatrix} \tag{A.1.14}$$

A.2 Seismic Representation theorem and Generalized Bremmer series

Seismic representation can be described as a special form of the reciprocity theorem [Fokkema and van den Berg, 1993], obtained if one of the acoustic wavefields represents the impulse response of a reference medium, i.e. Green's function whereas the other wavefield represents the physical wavefield in the true medium [Wapenaar and Berkhout, 1989]. Using the representation theorem, from the one-way wave equation derived in the previous section (in wavenumber-frequency domain), we have:

$$\partial_z \mathbf{P} = \mathbf{B}\mathbf{P} + \mathbf{S} \tag{A.2.15}$$

Further, similar to the above equation, we can also write the one-way wave equation for Green's function as:

$$\partial_z \mathbf{G} = \overline{\mathbf{B}}\mathbf{G} + \mathbf{I}\delta(z - z'), \tag{A.2.16}$$

where the source is located at z'. Using $\overline{\mathbf{B}} = \mathbf{\Lambda}$ and $\mathbf{B} = \mathbf{\Lambda} + \mathbf{\Theta}$, we have $\mathbf{B} - \overline{\mathbf{B}} = -\mathbf{L}^{-1}\partial_{\mathbf{z}}\mathbf{L} = \mathbf{\Theta}$, as mentioned in the previous section. Again, note that $\overline{\mathbf{B}}$ account for the primary-only wavefield propagation in the correct medium. Therefore, $\mathbf{G} = \mathbf{G_p}$, i.e. the Green's matrix for primaries. Now substituting this relationship is Equations (A.2.15) and (A.2.16), we get:

$$\partial_z \mathbf{P} - \Lambda\mathbf{P} = \mathbf{\Theta}\mathbf{P} + \mathbf{S} \tag{A.2.17}$$

and

$$\partial_z \mathbf{G}_p - \Lambda\mathbf{G}_p = \mathbf{I}\delta(z - z'). \tag{A.2.18}$$

Note that $\mathbf{G}_p(z, z')$ is the Green's matrix for primaries and can be written as:

$$\mathbf{G}_p(z, z') = \begin{bmatrix} H(z - z')\mathbf{W}^+(z, z') & \mathbf{0} \\ \mathbf{0} & -H(z - z')\mathbf{W}^-(z, z'), \end{bmatrix} \tag{A.2.19}$$

where $H(z)$ is the heavyside step-function, $\mathbf{W}^+$ and $\mathbf{W}^-$ are the upgoing and the downgoing propagation operators, as mentioned earlier (shown schematically in Figure A.2).

From Equations (A.2.17) and (A.2.18), we can write the wavefield at any depth z as a function of scattering matrix Θ and source term $\mathbf{S}$, as:

$$P(z) = \int \mathbf{G}_p(z, z') \left[\mathbf{\Theta}(z')P(z') + \mathbf{S}(z')\right] dz' \tag{A.2.20}$$

Splitting the equations for P^+ and P^-, we get:

$$\begin{aligned} P^{+(0)} &= \mathbf{W}^+\mathbf{S}^+, P^{-(0)} = \mathbf{W}^-\mathbf{S}^- \\ P^{+(k)} &= P^{+(0)} + \mathbf{W}^+[P^+ + R^{\cup}(P^+ - P^-)]^{(k-1)} \\ P^{-(k)} &= P^{-(0)} + \mathbf{W}^-[P^- + R^{\cup}(P^+ - P^-)]^{(k-1)}. \end{aligned} \tag{A.2.24}$$

Equation (A.2.24) is the same as the equation of the full wavefield model. They iteratively model the downgoing and the upgoing wavefield between two layers for a laterally invariant medium, as described in chapter two. Note again that for simplicity, the derivation in this appendix is shown in wavenumber-frequency domain, however, they can be generalized in space-frequency domain for 3D inhomogeneous medium.

Hence, in this appendix, we used to concepts of Seismic Representation theorem to describe an iterative modelling scheme which is termed as the Generalized Bremmer series [1]. In fact, it is equivalent to the iterative full-wavefield modelling scheme.

[1]Generalized Bremmer series reduces a complex scattering problem to a sequence of single scattering problems. In the Generalized Bremmer series, the wave equation is first decomposed into a coupled system of one-way wave equations. For more details on Bremmer series, the readers are referred to [Bremmer, 1951; Corones, 1975; Li, 1994; Gustafsson, 2000].

B

Matrix description used in this thesis

B.1 Extrapolation operators : W

The wavefield extrapolation operators in this thesis are based on the discrete Rayleigh integral. Using the acoustic wave equation and Green's theorem, we can derive the Kirchhoff integral, given by [Berkhout, 1981; Wapenaar and Berkhout, 1989; Gisolf and Verschuur, 2010]:

$$P(r_A,\omega) = \frac{-1}{4\pi}\int\limits_s \frac{1}{\rho(r)}\left[P(r,\omega)\frac{\partial G(r,r_A,\omega)}{\partial n} - \frac{\partial P(r,\omega)}{\partial n}G(r,r_A,\omega)\right]dS, \quad \text{(B.1.1)}$$

where P is the acoustic pressure in frequency domain, ρ is the mass density distribution, G is the Green's function and represents the pressure associated with the wavefield resulting from a point source in A, where A is an arbitrary point in a volume, enclosed by a surface S (as shown in Figure B.1).

Further, considering the surface seismic acquisition from one side and following the Sommerfield radiation principle, the closed Kirchhoff integral is simplified to an integral over a plane. The Kirchhoff integral can be used further to derive the Rayleigh integrals I and II using the Neumann boundary condition[1] and the Dirichlet boundary condition[2] for Green's function, respectively. We can split the total wavefield and the Green's function into the upgoing and the downgoing

[1]Neumann boundary condition: $\frac{\partial G}{\partial z} = 0$ at $z = z_0$
[2]Dirichlet boundary condition: $G = 0$ at $z = z_0$

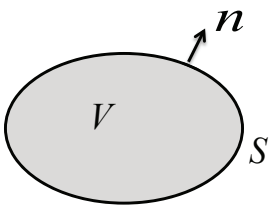

Figure B.1: *A bounded domain for deriving Kirchhoff integral.*

components, which satisfies the one-way wave equations as below:

$$\begin{array}{l} \frac{\partial P^+}{\partial z} + jH_1 * P^+ = 0 \\ \frac{\partial P^-}{\partial z} - jH_1 * P^- = 0 \\ \frac{\partial G^+}{\partial z} + jH_1 * G^+ = 0 \\ \frac{\partial G^-}{\partial z} - jH_1 * G^- = 0, \end{array} \tag{B.1.2}$$

where $P = P^+ + P^-$, $G = G^+ + G^-$ and for a laterally invariant velocity and density medium, $H_1(z_0)$ at the surface can be written as:

$$\widetilde{H}_1(k_x, k_y, z_0, \omega) = (x, y, x, \omega) e^{j(k_x x + k_y y)} dxdy = \sqrt{k^2(z_0) - k_x^2 - k_y^2}. \tag{B.1.3}$$

Further, by choosing the medium for the Green's function homogeneous above the surface, we get $G^+ = 0$. Using the one-way wavefield components in the Kirchhoff integral, we arrive to Rayleigh integral I:

$$P(r_A, \omega) = -\frac{1}{2\pi} \int\limits_s \frac{1}{\rho(r)} \frac{\partial P^+(r, \omega)}{\partial z} G^-(r, r_A, \omega) dS \tag{B.1.4}$$

and Rayleigh integral II:

$$P(r_A, \omega) = -\frac{1}{2\pi} \int\limits_s \frac{1}{\rho(r)} P^+(r, \omega) \frac{\partial G^-(r, r_A, \omega)}{\partial z} dS. \tag{B.1.5}$$

The above Rayleigh II integral in discrete form can be written as propagation of the downgoing wavefield from depth level z_n to z_{n+1} as:

$$P(z_{n+1}) = \mathbf{W}(z_{n+1}, z_n) P^+(z_n). \tag{B.1.6}$$

Further, one-way wavefield extrapolation operators are computed using the algorithm described in Thorbecke et al. [2004]. Wavefield extrapolation operator (as

shown in Figure B.2) in the wavenumber-frequency domain for a 2D medium is given by :

$$\widetilde{\mathrm{W}}(k_x, \omega, \Delta z) = e^{-jk_z \Delta z}, \tag{B.1.7}$$

where $k_z = \sqrt{k^2 - k_x^2}$ for $k_x^2 \leq k^2$ and $k_z = -j\sqrt{k_x^2 - k^2}$ for $k_x^2 > k^2$; k is define as ω/c, δz is a small extrapolation step, c is the propagation velocity of the layer, j is the imaginary unit, and ω is the angular frequency. This operator is same as the phase shift operator [Gazdag, 1978].

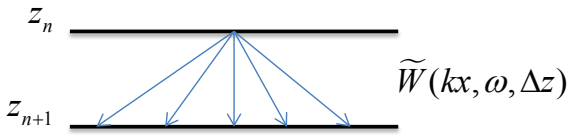

Figure B.2: *Schematic diagram showing the downward extrapolation operator.*

Note that for $k_x^2 > k^2$, the wavefield becomes evanescent i.e. exponentially decaying. For laterally varying media, the operator is applied as space-frequency convolution with the data to extrapolate it from depth level z_n to z_{n+1}. Further, the analytical inverse Fourier transform of equation (B.1.7) is a scaled Hankel function [Berkhout, 1984] given by:

$$\mathrm{W}(\mathrm{x}, \omega, \Delta \mathrm{z}) = -\mathrm{jk}\frac{\Delta \mathrm{z}}{2\mathrm{r}}\mathrm{H}_1^{(2)}(\mathrm{kr}), \tag{B.1.8}$$

where the distance $r = \sqrt{(x^2 + \Delta z^2)}$, $H_1^{(2)}(kr) = J_1(kr) - jY_1(kr)$ is the first-order Hankel function of the second kind, J_1 and Y_1 are the first-order Bessel functions of the first and second kind, respectively. Note that the inverse wavefield extrapolation operator F should invert for the wave propagation effects as $\widetilde{\mathrm{W}}\widetilde{\mathrm{F}} = \mathrm{I}$.

An inverse wavefield operator F for the phase shift operator is given by:

$$\widetilde{\mathrm{F}}(x, \omega, \Delta z) = \frac{1}{\widetilde{\mathrm{W}}(x, \omega, \Delta z)}. \tag{B.1.9}$$

The accuracy and stability should always be investigated for an inverse wavefield propagation operator. This inverse is accurate if $\widetilde{\mathrm{W}}\widetilde{\mathrm{F}} = \mathrm{I}$. However, for the evanescent part of the wavefield this inverse operator increases exponentially with Δz. Therefore it is not a stable operator. In order to stabilize the inverse operator, the following approximation is made $\widetilde{\mathrm{F}}(x, \omega, \Delta z) = \widetilde{\mathrm{W}}^H(x, \omega, \Delta z)$, where H represents the hermitian.

B.2 Reflectivity matrices $\mathbf{R}^{\cup}$ and $\mathbf{R}^{\cap}$

$\mathbf{R}^{\cup}(z_n)$ and $\mathbf{R}^{\cap}(z_n)$ represent reflectivity matrices related to a discontinuities at depth level z_n for the wavefield coming from above and from below the layer, respectively. The diagonal of the reflectivity matrices indicate the zero-offset reflection coefficients and the angle-dependent reflectivity information is contained in the full reflectivity matrices [see also de Bruin et al., 1990]. Consider two homogeneous acoustic half-spaces separated by an interface at z_n, then angle dependent reflection coefficient at a grid point, i.e. one element of the matrix $\mathbf{R}^{\cup}$ can be written as a function of incident angle α (shown in Figure B.3):

$$r^{\cup}(\alpha, z_n) = \frac{\rho_2 c_2 \cos\alpha - \rho_1 \sqrt{c_1^2 - c_2^2 \sin^2\alpha}}{\rho_2 c_2 \cos\alpha + \rho_1 \sqrt{c_1^2 - c_2^2 \sin^2\alpha}}. \tag{B.2.10}$$

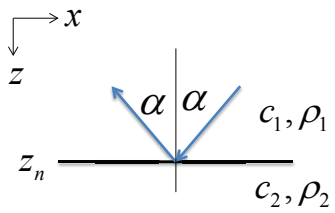

Figure B.3: *Reflection of an incident downgoing plane wave at an interface between two acoustic homogeneous half-spaces.*

Clearly we see that if $c_2 > c_1$, then the reflection function becomes complex for $sin|\alpha| > c_2/c_1$, i.e. $r^{\cup} = 1$ and total reflection occurs. We can define the critical angle as $\alpha_c = sin^{-}1(c_1/c_2)$. An example $r^{\cup}(\alpha)$ is plotted (courtesy of CREWES Zoeppritz explorer) for $c_1 = 1500m/s$, $c_1 = 3000m/s$ and $\rho_1 = \rho_2 = 1000m/s$.

Figure B.5 schematically illustrate the structure of the $\mathbf{R}$ matrix and illustrates an example of the angle-dependent and the angle-independent reflectivity vector in the space-time domain at a grid point located on a reflector.

Further, note also that for $\rho_1 \neq \rho_2$ and $c_1 = c_2$, the reflection coefficient becomes scalar i.e. angle-independent quantity. We can also write the expression for reflection coefficient for monochromatic plane waves as a function of horizontal wavenumber k_x, using $k_x = k_1 sin\alpha$ and $k_1 = \omega/c$, where ω is the angular frequency, given by $\omega = 2\pi f$, with f the frequency. Therefore the reflection

Bibliography

Abubakar, A., Hu, W., van den Berg, P. M., and Habashy, T. M., 2008, A finite-difference contrast source inversion method: Inverse Problems, **24**, 1–16.

Agnihotri, Y., and McMechan, G. A., 2007, Parsimonious migration of 3-C 3D VSP data: Geophysics, **72**, no. 6, S205–S213.

Aki, K., and Richards, P. G., 1980, Quantative seismology: W. H. Freeman and Co.

Al-Saleh, S. M., Margrave, G. F., and Gray, S. H., 2009, Direct downward continuation from topography using explicit wavefield extrapolation: Geophysics, **74**, no. 6, S105–S112.

Alá'i, R., and Wapenaar, C. P. A., 1994, Pseudo VSP generation from surface measurements : A new tool for seismic interpretation: J. Seis. Expl., **3**, no. 1, 79–94.

Alshuhail, A., Staal, X. R., and Verschuur, D. J., 2014, Incorporating anisotropy in joint migration inversion: 84nd Ann. Internat. Mtg., Soc. Expl. Geophys., Expanded abstracts.

Aminzadeh, F., and Mendel, J. M., 1982, Non-normal incidence state-space model and line-source reflection synthetic seismogram: Geophysical Prospecting, **30**, no. 5, 541–568.

Aminzadeh, F., and Mendel, J. M., 1985, Synthetic vertical seismic profiles for nonnormal incidence plane waves: Geophysics, **50**, no. 1, 127–141.

Aminzadeh, F., 1989, Application of elastic modelling in processing and interpretation of VSP data: a case history: Geophysical Prospecting, **37**, no. 8, 893–906.

Amundsen, L., 1991, Comparison of the least-squares criterion and the cauchy criterion in frequency-wavenumber inversion: Geophysics, **56**, no. 12, 2027–2035.

Amundsen, L., 1993, Depth imaging of offset vertical seismic profile data: Geophysical prospecting, **41**, no. 8, 1009–1031.

Arroyo, J. L., Breton, P., Dijkerman, H., Dingwall, S., Guerra, R., Hope, R., and Hornby, B., 2003, Superior seismic data from the borehole: Oilfield Review, **15**, no. 1, 2–23.

Bagaini, C., Daly, M., and Moore, I., 2012, The acquisition and processing of dithered slip-sweep vibroseis data: Geophys. Prosp., **60**, no. 4, 618–639.

Bai, J., and Yingst, D., 2013, Q estimation through waveform inversion: 75th Ann. Internat. Mtg., Eur. Ass. of Geosc. and Eng., Expanded abstracts.

Balch, A. H., Miller, M. W., and Ryder, R. T., 1982, The use of vertical seismic profiles in seismic investigations of the earth: Geophysics, **47**, no. 6, 906–918.

Barnes, C., and Charara, M., 2009, Viscoelastic full waveform inversion of north sea offset VSP data: 79th Ann. Internat. Mtg., Soc. Expl. Geophys., Expanded abstracts, 2278–2283.

Baysal, E., Kosloff, D. D., and Sherwood, J. W. C., 1983, Reverse time migration: Geophysics, **48**, no. 11, 1514–1524.

Beasley, C. J., Chambers, R. E., and Jiang, Z., 1998, A new look at simultaneous sources: 68th Ann. Internat. Mtg., Soc. Expl. Geophys., Expanded abstracts, 133–135.

Beasley, C. J., Dragoset, B., and Salama, A., 2012, A 3D simultaneous source field test processed using alternating projections: a new active separation method: Geophys. Prosp., **60**, no. 4, 591–601.

Behura, J., Wapenaar, K., and Snieder, R., 2012, Newton-Marchenko-Rose imaging: 82nd Ann. Internat. Mtg., Soc. Expl. Geophys., Expanded abstracts, 1–6.

Berkhout, A. J., and Verschuur, D. J., 1994, Multiple technology, part 2: Migration of multiple reflections: 64th Ann. Internat. Mtg., Soc. Expl. Geophys., Expanded abstracts, 1497–1500.

Berkhout, A. J., and Verschuur, D. J., 1997, Estimation of multiple scattering by iterative inversion, part I: theoretical considerations: Geophysics, **62**, no. 5, 1586–1595.

Berkhout, A. J., and Verschuur, D. J., 2004, Imaging multiple reflections, the concept: 74th Ann. Internat. Mtg., Soc. Expl. Geophys., Expanded abstracts, 1273–1276.

Berkhout, A. J., and Verschuur, D. J., 2005, Removal of internal multiples with the common-focus-point (CFP) approach: Part 1 - Explanation of the theory: Geophysics, **70**, no. 3, V45–V60.

Berkhout, A. J., and Verschuur, D. J., 2011, Full wavefield migration, utilizing surface and internal multiple scattering: 81th Ann. Internat. Mtg., Soc. Expl. Geophys., Expanded abstracts, 3212–3216.

Berkhout, A. J., Verschuur, D. J., and Blacquiére, G., 2012, Illumination properties and imaging promises of blended, multiple-scattering seismic data: a tutorial: Geophys. Prosp., **60**, no. 4, 713–732.

Berkhout, A. J., 1981, Wavefield extrapolation techniques in migration, a tutorial: Geophysics, **46**, no. 12, 1638–1656.

Berkhout, A. J., 1982, Seismic migration, imaging of acoustic energy by wave field extrapolation: Elsevier.

Berkhout, A. J., 1984, Seismic resolution: Geophysical press, London.

Berkhout, A. J., 1997, Pushing the limits of seismic imaging, part II: Integration of prestack migration, velocity estimation, and avo analysis: Geophysics, **62**, no. 3, 954–969.

Berkhout, A. J., 2008, Changing the mindset in seismic acquisition: The Leading Edge, **27**, no. 7, 924–938.

Berkhout, A. J., 2012, Combining full wavefield migration and full waveform inversion: Geophysics, **77**, no. 2, S43–S50.

Berkhout, A. J., 2014a, Review paper: An outlook on the future seismic imaging, part1: forward and reverse modelling: Geophysical Prospecting, **62**, no. 5, 911–930.

——— 2014b, Review paper: An outlook on the future seismic imaging, part2: Full-wavefield migration: Geophysical Prospecting, **62**, no. 5, 931–949.

——— 2014c, Review paper: An outlook on the future seismic imaging, part3: Joint migration inversion: Geophysical Prospecting, **62**, no. 5, 950–971.

Berryhill, J. R., and Kim, Y. C., 1986, Deep-water peg legs and multiples: Emulation and suppression: Geophysics, **51**, no. 12, 2177–2184.

Beylkin, G., Miller, D., and Oristaglio, M., 1987, The generalized radon transform: a breakthrough in seismic migration: The Technical Review, **35**, no. 3, 20–27.

Billette, F., and Brandsberg-Dahl, S., 2005, The 2004 BP velocity benchmark: 67th Ann. Internat. Mtg., Eur. Ass. of Geosc. and Eng., Expanded abstracts, B035.

Blias, E., 2008, Automatic 3-C 3-D VSP wavefield separation: 70th Ann. Internat. Mtg., Eur. Ass. of Geosc. and Eng., Expanded abstracts, H037.

Blias, E., 2012, Accurate interval Q-factor estimation from VSP data: Geophysics, **77**, no. 3, WA149–WA156.

Bouchon, M., and Aki, K., 1977, Discrete wavenumber representation of seismic source wave fields: Bull., Seis Soc. Am., **67**, no. 2, 259–277.

Bourbiè, T., and Serrano, A. G., 1983, Synthetic seismograms in attenuating media: Geophysics, **48**, no. 12, 1575–1587.

Bouska, J., 2010, Distance separated simultaneous sweeping, for fast, clean, vibroseis acquisition: Geophysical Prospecting, **58**, no. 1, 123–153.

Brand, E., Hurich, C., and Deemer, S., 2013, Geometrical considerations in the acquisition of borehole interferometric data for imaging near-vertical features: Design of field experiments: Geophysics, **78**, no. 3, K1–K10.

Brandsberg-Dahl, S., Gestel, J. P. V., Etgen, J. T., and Hornby, B., 2003, VSP salt flank imaging through wavefield continuation: 65th Ann. Internat. Mtg., Eur. Ass. of Geosc. and Eng., Expanded abstracts.

Bremmer, H., 1951, The W.K.B approximation as the first term of a geometric-optical series: Commun. Pure Appl. Math., **4**, 105–115.

Brown, M. P., and Guitton, A., 2005, Least-squares joint imaging of multiples and primaries: Geophysics, **70**, no. 5, S79–S89.

Buur, J., and Kühnel, T., 2008, Salt interpretation enabled by reverse time migration: Geophysics, **73**, no. 5, VE211–VE216.

Candès, E. J., and Tao, T., 2006, Near-optimal signal recovery from random projections: Universal encoding strategies: IEEE transactions on information theory, **52**, 5406–5425.

Cao, D., Beydoun, W. B., Singh, S. C., and Tarantola, A., 1990, A simultaneous inversion for background velocity and impedance maps: Geophysics, **55**, no. 4, 458–469.

Castagna, J. P., and Backus, M. M., 1993, Offset-dependent reflectivity - theory and practice of AVO analysis: Soc. of Expl. Geophys.

Cavalca, M., Moore, I., Zhang, L., Ng, S. L., Fletcher, R., and Bayly, M., 2011, Ray-based tomography for Q estimation and Q compensation in complex media: 81st Ann. Internat. Mtg., Soc. Expl. Geophys., Expanded abstracts, 3989–3993.

Cerjan, C., Kosloff, D., Kosloff, R., and Reshef, M., 1985, A nonreflecting boundary condition for discrete acoustic and elastic wave equations: Geophysics, **50**, no. 4, 705–708.

Chapman, C. H., 2004, Fundamentals of seismic wave propagation: Cambridge University Press.

Chen, G., Peron, J., and Canales, L., 2000, Rapid VSP-CDP mapping of 3-D VSP data: Geophysics, **65**, no. 5, 1631–1640.

Choi, Y., and Alkhalifah, T., 2012, Application of multi-source waveform inversion to marine streamer data using the global correlation norm: Geophys. Prosp., **60**, no. 4, 748–758.

Claerbout, J. F., and Muir, F., 1973, Robust modeling with erratic data: Geophysics, **38**, no. 5, 826–844.

Claerbout, J. F., 1976, Fundamental of geophysical data processing: Blackwell Scientific Publications.

Claerbout, J. F., 1985, Imaging the earth's interior: Blackwell Scientific Publications.

Coles, D., Yang, Y., Djikpesse, H., Prange, M., and Osypov, K., 2012, Optimal survey design for marine borehole seismics: 82nd Ann. Internat. Mtg., Soc. Expl. Geophys., Expanded abstracts, 1–5.

Corones, J., 1975, Bremmer series that correct parabolic approximations: Journal of Mathematical analysis and applications, **50**, 361–372.

Cosma, C., Balu, C., and Enescu, N., 2010, 3D VSP migration by image point transform: Geophysics, **75**, no. 3, S121–S130.

Dai, W., Fowler, P., and Schuster, G. T., 2012, Multi-source least-squares reverse time migration: Geophys. Prosp., **60**, no. 4, 681–695.

Daley, T. M., McEvilly, T. V., and Majer, E. L., 1988, Analysis of P and S wave vertical seismic profile data from the salton sea scientific drilling project: Journal of Geophysical Research, **93**, no. B11, 13025–13036.

Dankbaar, J. W. M., 1987, Vertical seismic profiling - separation of P- and S-waves: Geophysical Prospecting, **35**, no. 7, 803–814.

Dash, R., Spence, G., Hyndman, R., Grion, S., Wang, Y., and Ronen, S., 2009, Wide-area imaging from OBS multiples: Geophysics, **74**, no. 6, Q41–Q47.

Davydenko, M., and Verschuur, D. J., 2012, Demonstration of full wavefield migration in 2d subsurface models: 74th Ann. Internat. Mtg., Eur. Ass. of Geosc. and Eng., Expanded abstracts, P275.

Davydenko, M., and Verschuur, D. J., 2013, Full wavefield migration without dip limitation - using duplex waves in the imaging with multiples: 75th Ann. Internat. Mtg., Eur. Ass. of Geosc. and Eng., Expanded abstracts, We P02 09.

Davydenko, M., and Verschuur, D. J., 2014, Omnidirectional extension of full wavefield migration: 76th Ann. Internat. Mtg., Eur. Ass. of Geosc. and Eng., Expanded abstracts.

Davydenko, M., Staal, X. R., and Verschuur, D. J., 2012, Full wavefield migration in multidimensional media: 82nd Ann. Internat. Mtg., Soc. Expl. Geophys., Expanded abstracts, 1–5.

de Bruin, C. G. M., Wapenaar, C. P. A., and Berkhout, A. J., 1990, Angle-dependent reflectivity by means of prestack migration: Geophysics, **55**, no. 9, 1223–1234.

de Bruin, C. G. M., 1992, Linear avo inversion by prestack depth migration: Ph.D. thesis, Delft University of Technology.

Dean, T., Puckett, M., Quigley, J., Lane, D., and Tulett, J., 2013, Improving the low-frequency content of land VSP data acquired using a vibroseis source: Eur. Ass. of Geosc. and Eng., Expanded abstracts, Borehole Geophysics Workshop II, BGP01.

Dewangan, P., and Grechka, V., 2003, Inversion of multicomponent, multiazimuth, walkaway vsp data for the stiffness tensor: Geophysics, **68**, no. 3, 1022–1031.

Dey, A., and Gisolf, A., 2007, Wide-angle linear forward modelling of synthetic seismograms: Geophysical Prospecting, **55**, no. 5, 707–718.

Dietrich, M., and Bouchon, M., 1985, Synthetic vertical seismic profiles in elastic media: Geophysics, **50**, no. 2, 224–234.

Dillon, P. B., and Thomson, R. C., 1984, Offset source VSP surveys and their image reconstruction: Geophysical Prospecting, **632**, no. 5, 790–811.

Dillon, P. B., Ahmed, H., and Roberts, T., 1988, Migration of mixed-mode VSP wavefields: Geophysical Prospecting, **36**, no. 8, 825–846.

Dirks, V., Ma, X. Q., Randall, N., Blanco, J., Erbetta, M., and Gomes, J. L., 2002, High-resolution images from 4-C horizontal well VSP data: 72nd Ann. Internat. Mtg., Soc. Expl. Geophys., Expanded abstracts, 2341–2344.

DiSiena, J. P., Gaiser, J. E., and Corrigan, D., 1981, Three-component vertical seismic profile - orientation of horizontal components for shear wave analysis: 51st Ann. Internat. Mtg., Soc. Expl. Geophys., Expanded abstracts.

Dobrin, M. B., and Savit, C. H., 1988, Introduction to geophysical prospecting: 4th Edition, McGraw-Hill.

Donoho, D. L., 2006, Compressed sensing: IEEE transactions on information theory, **52**, 1289–1306.

Doulgeris, P., Bube, K., Hampson, G., and Blacquiére, G., 2012, Convergence analysis of a coherency-constrained inversion for the separation of blended data: Geophys. Prosp., **60**, no. 4, 769–781.

Doulgeris, P., 2013, Inversion methods for separation of blended data: Ph.D. thesis, Delft University of Technology.

Dragoset, B., Verschuur, E., Moore, I., and Bisley, R., 2010, A perspective on 3d surface-related multiple elimination: Geophysics, **75**, no. 5, 75A245–75A261.

Droujinine, A., 2005, Sub-basalt decoupled walkaway vsp imaging: Geophysical Prospecting, **53**, no. 1, 37–63.

Duijndam, A. J. W., Volker, A. W. F., and Zwartes, P. M., 2000, Acquisition footprint reduction - least squares migration versus reconstruction: 62th Ann. Internat. Mtg., Eur. Ass. of Geosc. and Eng., Expanded abstracts, P128.

Ferber, R. G., 1988, Time-domain computation of non-normal incidence wavefields in plane layered media: Geophysical Prospecting, **36**, no. 8, 857–877.

Fleury, C., 2013, Increasing illumination and sensitivity of reverse-time migration with internal multiples: Geophysical Prospecting, **61**, no. 5, 891–906.

Fokkema, J. T. ., and van den Berg, P. M., 1993, Seismic applications of acoustic reciprocity: Elsevier Science Publishers B.V.

Frasier, C. W., 1970, Discrete time solution of plane P-SV waves in a plane layered medium: Geophysics, **35**, no. 2, 197–219.

Friedlander, M. P., Mansour, H., Saab, R., and Yilmaz, O., 2012, Recovering compressively sampled signals using partial support information: IEEE transactions on information theory, **58**, no. 2, 1122–1134.

Fuchs, K., and Muller, G., 1971, Computation of synthetic seismograms with the reflectivity method and comparison of observations: Geoph. J. of the Royal Astronomical Soc., **23**, 417–433.

Fuller, B., Sterling, M., and Walter, L., 2006, Modern 2D and 3D VSP: reservoir imaging from downhole: First Break, **24**, no. 5, 63–68.

Futterman, W. I., 1962, Dispersive body waves: Journal of Geophysical research, **67**, 5279–5291.

Galis, M., Moczo, P., and Kristek, J., 2008, A 3-D hybrid finite-difference - finite-element viscoelastic modelling of seismic wave motion: Geophys. J. int., **175**, no. 1, 153–184.

Gal'perin, E. I., 1974, Vertical seismic profiling: SEG special publication nr. 12.

Gazdag, J., 1978, Wave equation migration with phase-shift method: Geophysics, **43**, no. 7, 1342–1351.

Geis, W. T., Stewart, R. R., Jones, M. J., and Katopodis, P. E., 1990, Processing, correlating, and interpreting converted shear waves from borehole data in southern alberta: Geophysics, **55**, no. 6, S241–S250.

Gherasim, M., 2005, 3-D VSP elastic kirchhoff pre-stack depth migration - vinton dome, louisiana: Ph.D. thesis, University of Houston.

Gilpatrick, R., and Fouquet, D., 1989, A user's guide to conventional VSP acquisition: The leading edge, **8**, no. 3, 34–39.

Gisolf, D., and Verschuur, D. J., 2010, The principles of quantitative acoustical imaging: EAGE Publications BV.

Grechka, V., and Mateeva, A., 2007, Inversion of P-wave VSP data for local anisotropy: theory and case study: Geophysics, **72**, no. 4, D69–D79.

Greenwood, A., Dupuis, C., Urosevic, M., and Kepic, A., 2012, Hydrophone VSP surveys in hard rock: Geophysics, **77**, no. 5, WC223–WC234.

Guerra, R., and Leaney, S., 2006, Q(z) model building using walkaway VSP data: Geophysics, **71**, no. 5, V127–V132.

Guitton, A., and Diaz, E., 2012, Attenuating crosstalk noise with simultaneous source full waveform inversion: Geophys. Prosp., **60**, no. 4, 759–768.

Guitton, A., Kaelin, B., and Biondi, B., 2007, Least-squares attenuation of reverse-time-migration artifacts: Geophysics, **72**, no. 1, S19–S23.

Gulati, J. S., Stewart, R. R., Peron, J., and Parkin, J. M., 1997, 3C-3D VSP: Normal moveout correction and VSPCDP transformation: CREWES research report, **9**, 1–30.

Gulati, J. S., Stewart, R. R., and Parkin, J. M., 2004, Analyzing three-component 3D vertical seismic profiling data: Geophysics, **69**, no. 2, 386–392.

Gulati, J. S., Salama, A., Leaney, S. W., Beasley, C. J., Coste, E., Menkiti, H., and Tulett, J., 2011, Faster 3D VSP acquisition using simultaneous sources: 81st Ann. Internat. Mtg., Soc. Expl. Geophys., Expanded abstracts, 4249–4252.

Gustafsson, M., 2000, The bremmer series for a multi-dimensional acoustic scattering problem: J. Phys. A: Math. Gen., **33**, no. 9, 1921–1932.

Haffinger, P., Gisolf, A., and van den Berg, P. M., 2013, Towards high resolution quantities subsurface models by full waveform inversion: Geophysical Journal International, **193**, 788–797.

Haffinger, P., 2013, Seismic broadband full waveform inversion: by shot / receiver refocusing: Ph.D. thesis, Delft University of Technology.

Haldorsen, J. B. U., Miller, D. E., and Walsh, J. J., 1995, Walkaway VSP using drill noise as a source: Geophysics, **60**, no. 4, 978–997.

Hardage, B. A., DeAngelo, M., and Murray, P., 2003, Defining P-wave and S-wave stratal surfaces with nine-component VSPs: The Leading Edge, **22**, no. 8, 720–729.

Hardage, B. A., 1985, Vertical seismic profiling, part A: prinicples: Geophysical Press.

Hargreaves, N. D., and Calvert, A. J., 1991, Inverse Q filtering by fourier transform: Geophysics, **56**, no. 4, 519–527.

Hartse, H., and Knapp, J. S., 1990, Understanding offset VSP: The Leading Edge, **9**, no. 4, 30–36.

Harwijanto, J. A., Wapenaar, C. P. A., and Berkhout, A. J., 1987, VSP migration by shot record inversion: First Break, **5**, no. 7, 247–255.

He, R., Hornby, B., and Schuster, G. T., 2006, 3D wave-equation interferometric migration of VSP multiples: 76th Ann. Internat. Mtg., Soc. Expl. Geophys., Expanded abstracts, 3442–3446.

Hendrickson, J. S., Kim, N. W., and Li, Y., 2011, PS salt proximity survey: The Leading Edge, **30**, no. 3, 258–264.

Hermann, P., and Wapenaar, C. P. A., 1992, Wave-type separation in the space-frequency domain applied to VSP data: Journal of Seismic Exploration, **1**, 161–172.

Hermann, F. J., Friedlander, M. P., and Yilmaz, O., 2012, Fighting the curse of dimensionality: compressive sensing in exploration seismology: IEEE Signal processing magazine, **29**, no. 3, 88–100.

Herrmann, F. J., and Li, X., 2012, Efficient least-squares migration with sparsity promotion and compressive sensing: Geophysical Prospecting, **60**, no. 4, 696–712.

Hestenes, M. R., and Stiefel, E., 1952, Methods of conjugate gradients for solving linear systems: J. Res. Natl. Bur. Stand., **49**, 409–436.

Hill, N. R., 1990, Gaussian beam migration: Geophysics, **55**, no. 11, 1342–1351.

Hindriks, C. O. H., and Duijndam, A. J. W., 1998, Radon domain reconstruction of 3d irregularly sampled VSP data: 68th Ann. Internat. Mtg., Soc. Expl. Geophys., Expanded abstracts, 2003–2006.

Hinds, R. C., Anderson, N. L., and Kuzmiski, R. D., 1996, VSP interpretive processing: theory and practice: Society of Exploration Geophysics.

Hokstad, K., Mittet, R., and Landral, M., 1988, Elastic reverse time migration of marine walkaway vertical seismic profiling data: Geophysics, **63**, no. 5, 1685–1695.

Hope, R., Ireson, D., Leaney, S., Meyer, J., Tittle, W., and Willis, M., 1998, Seismic integration to reduce risk: Oilfield Review, **10**, no. 3, 2–15.

Hornby, B. E., and Yu, J., 2007, Interferometric imaging of salt flank using walkaway vsp data: The Leading Edge, **26**, no. 6, 760–763.

Hornby, B. E., Yu, J., Sharp, J. A., Ray, A., Quist, Y., and Regone, C., 2006, VSP: Beyond time-to-depth: The Leading Edge, **25**, no. 4, 446–452.

Hou, S., Tsingas, C., Kelamis, P. G., Pecholcs, P. I., and Xu, H., 2012, Unconstrained simultaneous source land data processing: Geophys. Prosp., **60**, no. 4, 608–617.

House, N. J., Fuller, B., Behrman, D., and Allen, K. P., 2008, Acquisition, processing, and interpretation of a very large 3D VSP using new technologies: Risks tradeoffs and rewards: 78th Ann. Internat. Mtg., Soc. Expl. Geophys., Expanded abstracts, 3360–3364.

Howe, D., Foster, M., Allen, T., Taylor, B., and Jack, I., 2008, Independent simultaneous sweeping âĂŞ a method to increase the productivity of land seismic crews: 78th Ann. Internat. Mtg., Soc. of Expl. Geophys., Expanded abstracts, 2826–2830.

Huang, Y., and Schuster, G. T., 2012, Multi-source least-squares migration of marine streamer and land data with frequency-division encoding: Geophys. Prosp., **60**, no. 4, 663–680.

Ikelle, L. T., Erez, I., and Yang, X., 2009, Scattering diagrams in seismic imaging: More insights into the construction of virtual events and internal multiples: Journal of Applied Geophysics, **67**, no. 2, 150–170.

Ikelle, L. T., 2006, A construct of internal multiples from surface data only: the concept of virtual seismic events: Geophys. J. Int., **164**, no. 2, 383–393.

Ikelle, L. T., 2007, Coding and decoding: seismic data modeling, acquisition and processing: 77th Ann. Internat. Mtg., Soc. Expl. Geophys., Expanded abstracts, 66–70.

Jackson, G. M., Mason, I. M., and Lee, D., 1991, Multicomponent common-receiver gather migration of single-level walk-away seismic profiles: Geophysical prospecting, **39**, 1015–1029.

Jakubowicz, H., 1998a, Wave equation prediction and removal of interbed multiples: 60th Ann. Internat. Mtg., Eur. Ass. of Geosc. and Eng., Expanded abstracts, Session:1–28.

——— 1998b, Wave equation prediction and removal of interbed multiples: 68th Ann. Internat. Mtg., Soc. Expl. Geophys., Expanded abstracts, 1527–1530.

Jia, X., and Wu, R. S., 2009, Superwide-angle one-way wave propagator and its application in imaging steep salt flanks: Geophysics, **74**, no. 4, S75–S83.

Jiang, Z., and Abma, R., 2010, An analysis on the simultaneous imaging of simultaneous source data: 80th Ann. Internat. Mtg., Soc. Expl. Geophys., Expanded abstracts, 3115–3119.

Jiang, Z., Yu, J., Schuster, G. T., and Hornby, B. E., 2005, Migration of multiples: The Leading Edge, **24**, no. 3, 315–318.

Jiang, Z., Sheng, J., and Schuster, G., 2007, Migration methods for imaging different-order multiples: Geophysical Prospecting, **55**, no. 1, 1–19.

Jiang, Z., 2006a, Migration of interbed multiple reflections: 68th Ann. Internat. Mtg., Soc. Expl. Geophys., Expanded abstracts, 3501–3505.

——— 2006b, Multiple attenuation in VSP multiple imaging and primary imaging: 68th Ann. Internat. Mtg., Soc. Expl. Geophys., Expanded abstracts, 3477–3481.

Jin, S., Cambois, G., and Vuillermoz, C., 2000, Shear-wave velocity and density estimation from PS-wave AVO analysis: Application to an OBS dataset from the north sea: Geophysics, **65**, no. 5, 1446–1454.

Johnston, D. H., and Toksoz, M. N., 1980, Thermal cracking and amplitude dependent attenuation: J. Geophys. Res., **85**, 937–942.

Karrenbach, M., Soutyrine, V., and He, R., 2010, Combining standard salt/sediment-proximity analysis with interferometric imaging: 80th Ann. Internat. Mtg.

Keho, T. H., 1986, The vertical seismic profile: imaging heterogeneous media: Ph.D. thesis, Massachusetts Institute of Technology.

Kelly, K. R., Ward, R. W., Treitel, S., and Alford, R. M., 1976, Synthetic seismograms: A finite difference approach: Geophysics, **41**, no. 1, 2–27.

Kennett, B. L. N., 1979, Theoretical reflection seismograms for elastic media: Geophys. Prosp., **27**, no. 2, 301–321.

Kim, Y., Gruzinov, I., Guo, M., and Sen, S., 2009, Source separation of simultaneous source OBC data: 79th Ann. Internat. Mtg., Soc. Expl. Geophys., Expanded abstracts, 51–55.

Kiyashchenko, D., Mulder, W., and Lopez, J., 2009, Wave equation vector migration from subsalt VSP imaging and interpretation: 79th Ann. Internat. Mtg., Soc. Expl. Geophys., Expanded abstracts, 4134–4138.

Kjartansson, E., 1979, Constant Q, wave propagation and attenuation: J. Geophys. Res., **84**, 4737–4748.

Knopoff, L., and Gangi, A. F., 1959, Seismic reciprocity: Geophysics, **24**, no. 4, 681–691.

Kolsky, H., 1956, The propagation of stress pulses in viscoelastic solids: Philosophical magazine, **1**, 693–710.

Komatitsch, D., and Tromp, J., 1999, Introduction to the spectral element method for three-dimensional seismic wave propagation: Geophys. J. int., **139**, no. 3, 806–822.

Krasovec, M. L., 2001, Subsurface imaging with reverse vertical seismic profiles: Ph.D. thesis, Massachusetts Institute of Technology.

Krebes, E. S., and Hron, F., 1980, Ray-synthetic seismograms for SH waves in a layered anelastic media: SSA Bull., **70**, 2005–2020.

Kumar, A., Blacquière, G., and Verschuur, D. J., 2014a, 3-D acquisition geometry analysis: incorporating information from multiples: 84nd Ann. Internat. Mtg., Soc. Expl. Geophys., Expanded abstracts.

——— 2014b, Optimizing illumination using multiples: Application to seismic acquisition analysis: 76th Ann. Internat. Mtg., Eur. Ass. of Geosc. and Eng., Expanded abstracts.

Lailly, P., 1983, The seismic inverse problem as a sequence of before stack migrations: , Soc. of Industrial and Appl. Mathematics., Expanded abstracts, 206–220.

Leaney, W. S., Sacchi, M. D., and Ulrych, T. J., 2009, Least-squares migration with dip-field regularization: application to 3D VSP data: 79th Ann. Internat. Mtg., Soc. Expl. Geophys., Expanded abstracts, 2864–2868.

Leaney, K. S., 1990, Parametric wavefield decomposition and applications: 60th Ann. Internat. Mtg., Soc. of Expl. Geophys., Expanded abstracts, 1097–1100.

Lee, M. W., 1990, Traveltime inversion using transmitted waves of offset VSP data: Geophysics, **55**, no. 8, 1089–1097.

Lefeuvre, F., Nicoletis, L., Ansel, V., and Cliet, C., 1992, Detection and measure of the shear-wave birefringence from vertical seismic data: theory and applications: Geophysics, **57**, no. 11, 1463–1481.

Li, Y., Stewart, K., and Wang, D., 2005, Imaging of complex structures of salt flank using converted waves on 3-C VSP data: 67th Ann. Internat. Mtg., Eur. Ass. of Geosc. and Eng., Expanded abstracts.

Li, L., 1994, Bremmer series, R-matrix propagation algorithm, and numerical modeling of diffraction grating: J. Opt. Soc. Am. A, **11**, no. 11, 2829–2836.

Liang, L., Li, M., Rufino, R., Dümmong, S., Abubakar, A., Nutt, L., Tøndel, R., and Menkiti, H., 2013, Application of frequency-domain full-waveform inversion for time-lapse 3D VSP data interpretation in an extra heavy oil field: 83rd Ann. Internat. Mtg., Soc. Expl. Geophys., Expanded abstracts, 5107–5112.

Liao, Q., and McMechan, G. A., 1996, Multifrequency viscoacoustic modeling and inversion: Geophysics, **61**, no. 5, 1371–1378.

Lines, L. R., Bourgeois, A., and Covey, J. D., 1984, Traveltime inversion of offset vertical seismic profiles - a feasibility study: Geophysics, **49**, no. 3, 250–264.

Liu, T., Hu, T., Sen, M. K., Yang, J., Wang, R., Wei, J., and Wang, S., 2011a, A hybrid scheme for seismic modelling based on Galerkin method: Geophys. J. int., **186**, no. 3, 1165–1178.

——— 2011b, Reverse time migration of multiples for subsalt imaging: Geophysics, **76**, no. 5, WB209–WB216.

Lizarralde, D., and Swift, S., 1999, Smooth inversion of VSP traveltime data: Geophysics, **64**, no. 3, 659–661.

Lopez, G. A., and Verschuur, D. J., 2013, 3D primary estimation by sparse inversion using the focal domain parameterization: 83rd Ann. Internat. Mtg., Soc. Expl. Geophys., Expanded abstracts, 4172–4177.

Lou, M., Cheng, D., and Doherty, F., 2009, Suppressing VSP migration artifacts and noise by selected-aperture migration and damped: 79th Ann. Internat. Mtg., Soc. Expl. Geophys., Expanded abstracts, 4144–4148.

Lou, M., Campbell, M., Cheng, D., and Doherty, F., 2013, An improved parametric inversion methodology to decompose VSP P and Sv wavefields: 75th Ann. Internat. Mtg., Eur. Ass. of Geosc. and Eng., Expanded abstracts, We P11 02.

Lu, R., Willis, M., Campman, X., Franklin, J. A., and Toksoz, M. N., 2008, Redatuming through a salt canopy and target-oriented salt-flank imaging: Geophysics, **73**, no. 3, S63–S71.

Lu, R., Willis, M. E., Mateeva, A., Lopez, J., and Toksoz, M. N., 2009, Imaging a salt dome flank by directional redatuming of a field 3-D VSP survey: 79th Ann. Internat. Mtg., Soc. Expl. Geophys., Expanded abstracts.

Lu, S., Whitmore, N. D., Valenciano, A. A., and Chemingui, N., 2011, Imaging of primaries and multiples with 3D SEAM synthetic: 81th Ann. Internat. Mtg., Soc. Expl. Geophys., Expanded abstracts, 3217–3221.

Luo, Y., Liu, Q., Wang, Y. E., and AlFaraz, M. N., 2006, Imaging reflection-blind areas using transmitted PS-waves: Geophysics, **71**, no. 6, S241–S250.

MacBeth, C., Zeng, X., Li, X. Y., and Queen, J., 1995, Multicomponent near-surface correction for land VSP data: Geophys. J. Int., **121**, no. 1, 301–315.

MacBeth, C., Li, X. Y., Zeng, X., Cox, D., and Queen, J., 1997, Processing of a nine-component near-offset vsp for seismic anisotropy: Geophysics, **62**, no. 2, 676–689.

MacBeth, C., 2002, Multicomponent VSP analysis for applied seismic anisotropy, 1st ed.: Handbook of Geophysical Exploration, Seismic Exploration, Volume 26, Elsevier, UK.

Mahdad, A., Doulgeris, P., and Blacquiére, G., 2011, Separation of blended data by iterative estimation and subtraction of blending interference noise: Geophysics, **76**, no. 3, Q9–Q17.

Mahdad, A., Doulgeris, P., and Blacquiére, G., 2012, Iterative method for the separation of blended seismic data: discussion on the algorithmic aspects: Geophys. Prosp., **60**, no. 4, 782–801.

Mahdad, A., 2012, Deblending of seismic data: Ph.D. thesis, Delft University of Technology.

Majdański, M., Kostov, C., Kragh, E., Moore, I., Thompson, M., and Mispel, J., 2011, Attenuation of free-surface multiples by up/down deconvolution for marine towed-streamer data: Geophysics, **76**, no. 6, V129–V138.

Malcolm, A., de Hoop, M. V., and Calandra, H., 2007, Identifcation of image artifacts from internal multiples: Geophysics, **72**, no. 2, S123–S132.

Malcolm, A. E., Ursin, B., and de Hoop, M. V., 2008, Seismic imaging and illumination with internal multiples: Geophys. J. Int., **176**, no. 3, 847–864.

Mallick, S., and Frazer, L. N., 1988, Rapid computation of multioffset vertical seismic profile synthetic seismograms for layered media: Geophysics, **53**, no. 4, 479–491.

Mansour, H., Wason, H., Lin, T. T. Y., and Herrmann, F. J., 2012, Randomized marine acquisition with compressive sampling matrices: Geophysical Prospecting, **60**, no. 4, 648–662.

Mao, W., and Stuart, G. W., 1997, Transmission-reflection tomography: application to reverse VSP data: Geophysics, **62**, no. 3, 884–894.

Marhfoul, B. E., and Verschuur, D. J., 2014, Joint imaging of vsp and surface data: 84nd Ann. Internat. Mtg., Soc. Expl. Geophys., Expanded abstracts.

Mateeva, A., Mestayer, J., Yang, Z., Lopez, J., Willis, P., Roy, J., and Bown, T., 2013, Dual well 3D VSP in deepwater made possible by DAS: 83rd Ann. Internat. Mtg., Soc. Expl. Geophys., Expanded abstracts, 5062–5066.

McMechan, G. A., Hu, L. Z., and Stauber, D., 1988, Determination of salt proximity by wave-field imaging of transmitted energy: Geophysics, **53**, no. 8, 1109–1112.

McMechan, G. A., 1983, Migration by extrapolation of time-dependent boundary values: Geophysical prospecting, **31**, 413–420.

McMechan, G. A., 1985, Synthetic finite-offset vertical seismic profiles for laterally varying media: Geophysics, **50**, no. 4, 627–636.

Menke, W., 1984, Geophysical data analysis: direct inverse theory: Academic Press.

Miller, D., Oristaglio, M., and Beylkin, G., 1987, A new slant on seismic imaging: Migration and integral geometry: Geophysics, **52**, no. 7, 943–964.

Mittet, R., and Hokstad, K., 1995, Transforming walk-away VSP data into reverse VSP data: Geophysics, **60**, no. 4, 968–977.

Moldoveanu, N., Campbell, A., and Meyer, J., 2000, High fidelity vibratory seismic applications for VSP: 70th Ann. Internat. Mtg., Soc. Expl. Geophys., Expanded abstracts, 1759–1762.

Moore, I., Dragoset, W., Ommundsen, T., Wilson, D., Ward, C., and Eke, D., 2008, Simultaneous source separation using dithered sources: 78th Ann. Internat. Mtg., Soc. Expl. Geophys., Expanded abstracts, 2806–2809.

Moret, G. J. M., Clement, W. P., Knoll, M. D., and Barrash, W., 2004, VSP traveltime inversion: near-surface issues: Geophysics, **69**, no. 2, 345–351.

Morley, L. C., 2013, Application of compressive sensing to 3D-VSP acquisition and processing: Eur. Ass. of Geosc. and Eng., Expanded abstracts, Borehole Geophysics Workshop II, BG14.

Müller, K. W., Soroka, W. L., Paulsson, B. N. P., Marmash, S., Baloushi, M. A., and Jeelani, O. A., 2010a, 3D VSP technology now a standard high-resolution reservoir imaging technique: Part1, acquisition and processing: The Leading Edge, **29**, no. 6, 686–697.

——— 2010b, 3D VSP technology now a standard high-resolution reservoir imaging technique: Part2, interpretation and value: The Leading Edge, **29**, no. 6, 698–704.

Nasyrov, D., Kiyashchenko, D., Kiselev, Y., Kashtan, B., and Troyan, V., 2009, Multiple migration of VSP data for velocity analysis: 79th Ann. Internat. Mtg., Soc. Expl. Geophys., Expanded abstracts, 4164–4168.

Nawaz, M. A., and Borland, W. H., 2013, Simulation and proposed processing workflow of simultaneous source 3D-VSP data: Eur. Ass. of Geosc. and Eng., Expanded abstracts, Borehole Geophysics Workshop II, BG27.

Neelamani, R., Krohn, C. E., Krebs, J. R., Romberg, J. K., Deffenbaugh, M., and Anderson, J. E., 2010, Efficient seismic forward modeling using simultaneous random sources and sparsity: Geophysics, **75**, no. 6, WB15–WB27.

Neklyudov, D., and Borodin, I., 2009, Imaging of offset VSP data acquired in complex areas with modified reverse-time migration: Geophysical Prospecting, **57**, no. 3, 379–391.

Nemeth, T., Wu, C., and Schuster, G. T., 1999, Least-squares migration of incomplete reflection data: Geophysics, **64**, no. 1, 208–221.

O'Brien, J., Mallick, B., and Lakings, J., 2002, Locating the salt flank using borehole seismic techniques: 72nd Ann. Internat. Mtg., Soc. Expl. Geophys., Expanded abstracts, 2345–2348.

O'Brien, J., Farmani, B., and Atkinson, B., 2013a, VSP free-surface multiple imaging - a detailed case study: 75th Ann. Internat. Mtg., Eur. Ass. of Geosc. and Eng., Expanded abstracts, Th 17 14.

——— 2013b, VSP imaging using free-surface multiples: A case study from Gulf of Mexico: The Leading Edge, **32**, no. 10, 1258–1266.

O'Brien, J., 2005, The sediment proximity survey, or how to find the salt flank: The Leading Edge, **24**, no. 4, 415–420.

Oldenburg, D. W., Scheuer, T., and Levy, S., 1983, Recovery of the acoustic impedance from reflection seismograms: Geophysics, **48**, no. 10, 1318–1337.

Omnes, G., 1980, Logs from P and S vertical seismic profiles: Petroleum Technology, **32**, 1843–1849.

Oristaglio, M. L., 1985, A guide to the current uses of vertical seismic profiles: Geophysics, **50**, no. 12, 2473–2479.

Palacios, N. A., Planchart, C. A., and Jiao, J., 2013, Efficient wavefield separation for large 3D VSPs in saudi arabia: Eur. Ass. of Geosc. and Eng., Expanded abstracts, Borehole Geophysics Workshop II, BG04.

Payne, M. A., Eriksen, E. A., and Rape, T. D., 1990, Considerations for high-resolution VSP imaging: The Leading Edge, **9**, no. 4, 30–36.

Pereira, A. M., and Jones, M., 2010, Fundamentals of borehole seismic technology: Schlumberger Oilfield Marketing Communications.

Plessix, R. E., Baeten, G., de Maag, J. W., ten Kroode, F., and Ruijie, Z., 2012, Full waveform inversion and distance separated simultaneous sweeping: a study with a land seismic data set: Geophys. Prosp., **60**, no. 4, 733–747.

Podgornova, O., Owusu, J. C., Charara, M., Leaney, S., Campbell, A., Ali, S., Borodin, I., Nutt, L., and Menkit, H., 2013a, Anisotropic elastic full-waveform inversion for a real walkaway vsp data from the arabian gulf -towards high frequencies: 75th Ann. Internat. Mtg., Eur. Ass. of Geosc. and Eng., Expanded abstracts, Th 10 08.

——— 2013b, Anisotropic full waveform inversion of walkaway vsp data from the arabian gulf: Eur. Ass. of Geosc. and Eng., Expanded abstracts, Borehole Geophysics Workshop II, BG20.

Polak, E., and Ribiére, G., 1969, Note sur la convergence de directions conjugÃľes: Rev. Francaise Informat Recherche Opertionelle, **16**, 35–43.

Poster, C., 1983, A comparison of seismic sources for VSP's in a cased well: Journal of the Canadian soc. of Expl. Geophysicists, **19**, no. 1, 34–43.

Protasov, M. I., and Tcheverda, V. A., 2012, True amplitude elastic gaussian beam imaging of multicomponent walkaway vertical seismic profiling data: Geophysical Prospecting, **60**, no. 6, 1030–1042.

Ravasi, M., and Curtis, A., 2013, Nonlinear scattering based imaging in elastic media: Theory, theorems, and imaging conditions: Geophysics, **78**, no. 3, S137–S155.

Reshef, M., Arad, S., and Landa, E., 2006, 3D prediction of surface-related and interbed multiples: Geophysics, **71**, no. 1, V1–V6.

Rizzuti, G., and Gisolf, D., 2014a, 2-D wavefield inversion for high-resolution elastic property estimation: 76th Ann. Internat. Mtg., Eur. Ass. of Geosc. and Eng., Expanded abstracts.

——— 2014b, Elastic wavefield inversion of seismic reflection data for high-resolution near surface characterization: 82nd Ann. Internat. Mtg., Soc. Expl. Geophys., Expanded abstracts, 2066–2071.

Robinson, J. C., 1979, A technique for continuous representation of dispersion on seismic data: Geophysics, **44**, 1245–1351.

Ross, W. S., and Shah, P. M., 1987, Vertical seismic profile reflectivity: Ups over downs: Geophysics, **52**, no. 8, 1149–1154.

Sacchi, M. D., Ulrych, T. J., and Walker, C. J., 1998, Interpolation and extrapolation using a high-resolution discrete fourier transform: IEEE Trans. Signal Processing, **46**, no. 1, 31–38.

Sandberg, K., and Beylkin, G., 2009, Full-wave-equation depth extrapolation for migration: Geophysics, **74**, no. 6, WCA121–WCA128.

Sava, P., and Guitton, A., 2005, Multiple attenuation in the image space: Geophysics, **70**, no. 1, V10–V20.

Schneider, W. A., 1978, Integral formulation for migration in two and three dimensions: Geophysics, **43**, no. 1, 49–76.

Sheley, D., and Schuster, G. T., 2003, Reduced-time migration of transmitted PS waves: Geophysics, **68**, no. 5, 1695–1707.

Sherrif, R. E., 2002, Enclyclopedic dictionary of applied geophysics: Society of Exploration Geophysicists.

Shin, C., 1995, Sponge boundary condition for frequency-domain modeling: Geophysics, **60**, no. 6, 1870–1874.

Shuey, R. T., 1985, A simplification of the Zoeppritz equations: Geophysics, **50**, no. 4, 609–614.

Silvestrov, I., Neklyudov, D., Kostov, C., and Tcheverda, V., 2013, Full-waveform inversion for macro velocity model reconstruction in look-ahead offset vertical seismic profile: numerical singular value decomposition-based analysis: Geophysical Prospecting, **61**, no. 6, 1099–1113.

Slob, E., Wapenaar, K., Broggini, F., and Snieder, R., 2014, Seismic reflector imaging using internal multiples with Marchenko-type equations: Geophysics, **79**, no. 2, S63–S76.

Snieder, R., Xie, M. Y., Pica, A., and Tarantola, A., 1989, Retrieving both the impedance contrast and background velocity: A global strategy for the seismic reflection problem: Geophysics, **54**, no. 8, 991–1000.

Soni, A. K., and Verschuur, D. J., 2013a, Full wavefield migration of vertical seismic profiling data: Using all multiples for imaging away from the well: Eur. Ass. of Geosc. and Eng., Expanded abstracts, Borehole Geophysics Workshop II, BG10.

——— 2013b, Imaging blended VSP data using full wavefield migration: 83rd Ann. Internat. Mtg., Soc. of Expl. Geophys., Expanded abstracts, 5046–5051.

——— 2013c, Imaging vertical seismic profiling data using full wavefield migration: 75th Ann. Internat. Mtg., Eur. Ass. of Geosc. and Eng., Expanded abstracts, Th 17 11.

Soni, A. K., and Verschuur, D. J., 2014a, Full wavefield migration of vertical seismic profiling data: using all multiples to extend the illumination area: Geophysical Prospecting, **62**, no. 4, 740–759.

——— 2014b, Imaging of blended vsp data using full wavefield migration in the common-receiver domain: 76th Ann. Internat. Mtg., Eur. Ass. of Geosc. and Eng., Expanded abstracts.

Soni, A. K., Staal, X. R., and Verschuur, D. J., 2012a, Estimation of surface impulse response data from walkaway VSP measurements: 74th Ann. Internat. Mtg., Eur. Ass. of Geosc. and Eng., Expanded abstracts, A026.

——— 2012b, VSP imaging using all multiples: Full wavefield migration approach: 82nd Ann. Internat. Mtg., Soc. of Expl. Geophys., Expanded abstracts, 1–6.

——— 2012c, Target oriented VSP imaging - a sparse-inversion approach: 74th Ann. Internat. Mtg., Eur. Ass. of Geosc. and Eng., Expanded abstracts, P095.

Spitz, S., Hampson, G., and Pica, A., 2008, Simultaneous source separation: A prediction-subtraction approach: 78th Ann. Internat. Mtg., Soc. Expl. Geophys., Expanded abstracts, 2811–2814.

Staal, X. R., and Verschuur, D. J., 2012, Velocity estimation using internal multiples: 82nd Ann. Internat. Mtg., Soc. of Expl. Geophys., Expanded abstracts, 1–5.

Staal, X. R., and Verschuur, D. J., 2013, Joint migration inversion, imaging including all multiples with automatic velocity update: 75th Ann. Internat. Mtg., Eur. Ass. of Geosc. and Eng., Expanded abstracts, Tu 02 16.

Staal, X. R., Verschuur, D. J., and Berkhout, A. J., 2014, Robust velocity estimation by joint migration inversion: 76th Ann. Internat. Mtg., Eur. Ass. of Geosc. and Eng., Expanded abstracts, We G103 07.

Stewart, R. R., Gaiser, J. E., Brown, R. J., and Lawton, D. C., 2002, Converted-wave seismic exploration: Methods: Geophysics, **67**, no. 5, 1348–1363.

Stewart, R. R., 1983, Vertical seismic profiling: the one-dimensional forward and inverse problems: Ph.D. thesis, Massachusetts Institute of Technology.

Strang, G., 2003, Introduction to linear algebra: Wellsley-Cambridge Press.

Sun, R., and McMechan, G. A., 1986, Pre-stack reverse-time migration for elastic waves with application to synthetic offset vertical seismic profiles: Proceedings of IEEE, **74**, no. 3, 457–465.

Sun, W., Sun, S. Z., and Bai, H., 2009, 3C-3D VSP vector field wavefield separation with constrained inversion: 79th Ann. Internat. Mtg., Soc. of Expl. Geophys., Expanded abstracts, 4080–4084.

Suprajitno, M., and Greenhalgh, S. A., 1986, Theoretical vertical seismic profiling: Geophysics, **51**, no. 6, 1252–1265.

Tan, S., and Huang, L., 2014, Least-squares reverse-time migration with a wavefield-separation imaging condition and updated source wavefields: Geophysics, **79**, no. 5, S195–S205.

Tang, Y., and Biondi, B., 2009, Least-squares migration/inversion of blended data: 79tht Ann. Internat. Mtg., Soc. Expl. Geophys., Expanded abstracts, 2859–2863.

Tarantola, A., 1986, A strategy for nonlinear elastic inversion of seismic reflection data: Geophysics, **51**, no. 10, 1893–1903.

Tarantola, A., 1987, Inverse problem theory, methods for data fitting and model parameter estimation: Elsevier Science Publ. Co., Inc.

Telford, W. M., Geldart, L. P., Sheriff, R. E., and Keys, D. A., 1990, Applied geophysics: 2nd Edition, Cambridge University Press.

ten Kroode, F., Bergler, S., Corsten, C., de Maag, J. W., Strijbos, F., and Tijhof, H., 2013, Broadband seismic data - the importance of low frequencies: Geophysics, **78**, no. 2, WA3–WA14.

ten Kroode, A. P. E., 2002, Prediction of internal multiples: Wave Motion, **35**, 315–338.

Thorbecke, J. W., Wapenaar, K., and Swinnen, G., 2004, Design of one-way wavefield extrapolation operators, using smooth functions in WLSQ optimization: Geophysics, **69**, no. 4, 1037–1045.

Toverud, T., and Ursin, B., 2005, Comparison of seismic attenuation models using zero-offset vertical seismic profiling (VSP) data: Geophysics, **70**, no. 2, F17–F25.

Ursin, B., 1983, Review of elastic and electromagnetic wave propagation in horizontally layered media: Geophysics, **48**, no. 8, 1063–1081.

van Borselen, R., Baardman, R., Martin, T., Goswami, B., and Fromyr, E., 2012, An inversion approach to separating sources in marine simultaneous shooting acquisition - application to a Gulf of Mexico data set: Geophys. Prosp., **60**, no. 4, 640–647.

van den Berg, P. M., and Kleinman, R. E., 1997, A contrast source inversion method: Inverse Problems, **13**, no. 6, 1607–1620.

van den Berg, P. M., van Broekhoven, A. L., and Abubakar, A., 1999, Extended contrast source inversion: Inverse Problems, **15**, no. 5, 1325–1344.

van Gestel, J. P., Hornby, B., and Roy, A., 2002, VSP survey design using finite difference modeling: 72nd Ann. Internat. Mtg., Soc. Expl. Geophys., Expanded abstracts, 2361–2365.

van Groenestijn, G. J. A., and Verschuur, D. J., 2008, Towards a new approach for primary estimation: 78th Ann. Internat. Mtg., Soc. Expl. Geophys., Expanded abstracts, 2487–2491.

van Groenestijn, G. J. A., and Verschuur, D. J., 2009a, Estimating primaries by sparse inversion and application to near-offset data reconstruction: Geophysics, **74**, no. 3, A23–A28.

——— 2009b, Estimation of primaries and near offsets by sparse inversion: Marine data applications: Geophysics, **74**, no. 6, R119–R128.

Varela, C. L., Rosa, A. L. R., and Ulrych, T. J., 1993, Modelling of attenuation and dispersion: Geophysics, **58**, no. 8, 1167–1173.

Vasconcelos, I., Snieder, R., and Hornby, B., 2008, Imaging internal multiples from subsalt VSP data - examples of target-oriented interferometry: Geophysics, **73**, no. 4, S157–S168.

Verschuur, D. J., and Berkhout, A. J., 2005, Removal of internal multiples with the common-focus-point (CFP) approach: Part 2 - Application strategies and data examples: Geophysics, **70**, no. 3, V61–V72.

Verschuur, D. J., and Berkhout, A. J., 2009, Target-oriented, least-squares imaging of blended data: 79th Ann. Internat. Mtg., Soc. Expl. Geophys., Expanded abstracts, 2889–2893.

Verschuur, D. J., and Berkhout, A. J., 2011, Seismic migration of blended shot records with surface-related multiple scattering: Geophysics, **76**, no. 1, A7–A13.

Verschuur, D. J., Berkhout, A. J., and Wapenaar, C. P. A., 1992, Adaptive surface-related multiple elimination: Geophysics, **57**, no. 9, 1166–1177.

Verschuur, D. J., Vrolijk, J. W., and Tsingas, C., 2012, 4D reconstruction of wide azimuth (WAZ) data using sparse inversion of hybrid radon transforms: 82nd Ann. Internat. Mtg., Soc. Expl. Geophys., Expanded abstracts, 1–6.

Verschuur, D. J., 1991, Surface-related multiple elimination: an inversion approach: Ph.D. thesis, Delft University of Technology.

Verschuur, D. J., 2006, Seismic multiple removal techniques - past, present and future: EAGE Publications BV.

Virieux, J., and Operto, S., 2009, An overview of full-waveform inversion in exploration geophysics: Geophysics, **74**, no. 6, WCC127 – WCC152.

Virieux, J., 1986, P-SV wave propagation in heterogeneous media: Velocity-stress finite difference method: Geophysics, **51**, no. 4, 889–901.

von Steht, M., 2008, Imaging of vertical seismic profiling data using the common-reflection-surface stack: Ph.D. thesis, Karlsruhe Institute of Technology.

Wang, J., and Sacchi, M. D., 2007, High-resolution wave-equation amplitude-variation-with-ray-parameter (AVP) imaging with sparseness constraints: Geophysics, **72**, no. 1, S11–S18.

Wang, Y., 2002, A stable and efficient approach of inverse Q filtering: Geophysics, **67**, no. 2, 657–663.

Wang, Y., 2004, Multiple prediction through inversion: A fully data-driven concept for surface-related multiple attenuation: Geophysics, **69**, no. 2, 547–553.

Wang, Y., 2006, Inverse Q filter for seismic resolution enhancement: Geophysics, **71**, no. 3, V51–V60.

Wang, Y., 2008, Inverse Q filtered migration: Geophysics, **73**, no. 1, S1–S6.

Wang, Y., 2014, Stable Q analysis on vertical seismic profiling data: Geophysics, **79**, no. 4, D217–D225.

Wapenaar, C. P. A., and Berkhout, A. J., 1989, Elastic wave field extrapolation: redatuming of single- and multi-component seismic data: Elsevier Science Publ. Co., Inc.

Wapenaar, C. P. A., and Grimbergen, J. L. T., 1996, Reciprocity theorems for one-way wavefields: Geophys. J. Int, **127**, 169–177.

Wapenaar, C. P. A., and Haime, G. C., 1990, Elastic extrapolation pf primary seismic P- and S-waves: Geophys. Prosp., **38**, 23–60.

Wapenaar, K., van der Neut, J., and Thorbecke, J., 2012, Deblending by direct inversion: Geophysics, **77**, no. 3, A9–A12.

Wapenaar, K., Slob, E., van der Neut, J., Thorbecke, J., Broggini, F., and Snieder, R., 2013, Three-dimensional Marchenko equation for Green's function retrieval "beyond seismic interferometry": 83rd Ann. Internat. Mtg., Soc. of Expl. Geophys., Expanded abstracts, 4573–4578.

Wapenaar, K., Thorbecke, J., van der Neut, J., Broggini, F., Slob, E., and Snieder, R., 2014, Marchenko imaging: Geophysics, **79**, no. 3, WA39–WA45.

Wapenaar, C. P. A., 1996a, One-way representations of seismic data: Geophys. J. Int, **127**, 178–188.

——— 1996b, Reciprocity theorems for two-way and one-way wave vectors: a comparison: J. Acoust. Soc. Am., **100**, no. 6, 3508–3518.

Warner, M., Ratcliffe, A., Nangoo, T., Morgan, J., Umpleby, A., Shah, N., Vinje, V., Stekl, I., Guasch, L., Win, C., Conroy, G., and Bertrand, A., 2013, Anisotropic 3D full-waveform inversion: Geophysics, **78**, no. 2, R59–R80.

Weglein, A. B., Gasparotto, F. A., Carvalho, P. M., and Stolt, R. H., 1997, An inverse scattering series method for attenuating multiples in seismic reflection data: Geophysics, **62**, 1975–1989.

Whitmore, N. D., and Lines, L. R., 1986, Vertical seismic profiling depth migration of a salt dome flank: Geophysics, **51**, no. 5, 1087–1109.

Willis, M., Lu, R., , Campman, X., Toksoz, M. N., and de Hoop, M. V., 2006, A novel application of time-reversed acoustics: Salt-dome flank imaging using walkaway VSP surveys: Geophysics, **71**, no. 2, A7–A11.

Wyatt, K. D., 1981, Synthetic vertical seismic profile: Geophysics, **46**, no. 6, 880–891.

Xiao, X., and Schuster, G. T., 2009, Local migration with extrapolated VSP green's functions: Geophysics, **74**, no. 1, SI15–SI26.

Xiao, X., Zhou, M., and Schuster, T., 2003, Salt-flank delineation by interferometric imaging of transmitted P- to S-waves: Geophysics, **68**, no. 5, 1695–1707.

Xu, C., and Stewart, R. R., 2004, Using 3D multi-component seismic data, logs and VSP to interpret a sand-shale oil reservoir: 66th Ann. Internat. Mtg., Eur. Ass. of Geosc. and Eng., Expanded abstracts, Z–99.

Xu, X., 1990, Downhole synthetic seismic profiles in elastic media: Geophysical Prospecting, **38**, no. 2, 139–168.

Yan, Y., Xu, Z., Li, M., and Wei, X., 2012, Application of 3D vertical seismic profile multi-component data to tight gas sands: Geophysical prospecting, **60**, no. 1, 138–152.

Yao, G., and Jakubowicz, H., 2012a, Least-squares reverse-time migration: 82nd Ann. Internat. Mtg., Soc. Expl. Geophys., Expanded abstracts, 1–5.

——— 2012b, Non-linear least-squares reverse-time migration: 82nd Ann. Internat. Mtg., Soc. Expl. Geophys., Expanded abstracts, 1–5.

Youn, O. K., and Zhou, H. W., 2001, Depth imaging with multiples: Geophysics, **66**, no. 1, 246–255.

Young, T. K., Monash, C. B., and Turpening, R. M., 1984, Computer modelling of vertical seismic profiling: Geophysical Prospecting, **32**, 851–870.

Yu, J., and Hornby, B., 2008, A strategy for attenuating VSP migration artefacts: local beam migration: 78th Ann. Internat. Mtg., Soc. Expl. Geophys., Expanded abstracts, 3385–3389.

Zhang, R., and Castagna, J., 2011, Seismic sparse-layer reflectivity inversion using basis pursuit decomposition: Geophysics, **76**, no. 6, R147–R158.

Zhang, J., and McMechan, G. A., 1997, Turning wave migration by horizontal extrapolation: Geophysics, **62**, no. 1, 291–296.

Zhang, Y., and Sun, J., 2009, Practical issues in reverse time migration: true amplitude gathers, noise removal and harmonic source encoding: Leading edge, **26**, 29–35.

Zhang, Y., Duan, L., and Xie, Y., 2014a, Correlative least-squares time migration and its applications: 76th Ann. Internat. Mtg., Eur. Ass. of Geosc. and Eng., Expanded abstracts.

——— 2014b, Amplitude-preserving reverse time migration: from reflectivity to velocity and impedance inversion: Geophysics, **79**, no. 6, S271–S283.

Zhao, X., Li, Y., and Doherty, F., 2006, Imaging of steep salt face and surrounding sediments using vertical seismic profile (VSP) converted waves: 76th Ann. Internat. Mtg.

Zheng, D., and Schuster, G. T., 2014, Least-squares reverse time migration of multiples: Geophysics, **79**, no. 1, S11–S21.

Zhou, B., and Greenhalgh, S. A., 1994, Wave-equation extrapolation-based multiple attenuation: 2-D filtering in the F-K domain: Geophysics, **59**, no. 10, 1377–1391.

Zhu, X., and McMechan, G. A., 2011, Comparison of methods for modeling phase variation with angle: 81st Ann. Internat. Mtg., Soc. Expl. Geophys., Expanded abstracts, 3053–3058.

Summary

Until now, in most seismic imaging technologies, both surface and internal multiples are considered as noise. In today's industrial practice, we see various methods for suppressing multiples before migration. This means that only a fraction of the recorded wavefield is used in imaging. In this thesis, we present a method termed full wavefield migration (FWM) that uses the multiple-reflections in the data to improve the illumination of the field in areas that cannot be reached by the primaries, to yield a better vertical resolution as well as to suppress migration artefacts caused by crosstalk of multiple-reflections.

This thesis demonstrates the feasibility of full wavefield migration on a kind of borehole seismic known as vertical seismic profiling (VSP). We know that in today's practice, images obtained using VSP data always suffer from poor illumination and small aperture effects. Therefore, we expect in VSP acquisition geometry, multiples can lead to significant improvement in illumination, both at the reservoir level as well as away from the well region. In this thesis, the advantage of using multiples in full wavefield migration has been demonstrated. We validated our algorithm on 2D synthetic and field VSP data.

Full wavefield migration is posed as an inverse problem, where the parameters to be estimated are the subsurface reflectivities. We discuss an iterative forward modelling engine termed full wavefield modelling which is used in the inversion scheme. Full wavefield modelling allows us to compute the full wavefield (primaries and all multiples) in terms of estimated reflectivities. In the full wavefield modelling engine, we assume a scale-separation between the background migration velocity that governs only the one-way wavefield propagation and the reflectivity model that governs the two-way scattering. The modelling engine accounts for the non-linearity of the wavefield due to reflectivity, incorporating the transmission effects and multiple scattering at all depth levels. To solve the inverse problem, we have used iterative conjugate-gradient scheme, which is a local optimization method.

We also presents a solution for imaging of blended source VSP data using FWM. The inversion-based imaging algorithm allows us to use any complex source wavefield without the need for a separate deblending (pre-processing) step. This thesis introduces the concepts of elastic full wavefield modelling and inversion. The elastic modelling of P and S waves is illustrated for a horizontally layered medium using a VSP geometry. The elastic imaging to estimate angle-dependent reflectivity parameters that incorporates mode-conversions in subsurface layers is an important area of future research. Nearly vertical structures such as salt-flanks pose a migration challenge for conventional FWM. We have also extended the FWM algorithm to incorporate turning-waves using horizontal one-way wavefield extrapolation. Using this extension, we illustrate that FWM can be used to image steep dips or near-vertical structures using the turning wavefield in VSP data.

Alok Kumar Soni.

Samenvatting

Tot nu toe worden zowel surface en interne multiples door de meeste seismische afbeeldingstechnieken als ruis behandeld. In de huidige industriële praktijk zien we diverse methodes om multiples te onderdrukken voor migratie. Dit betekent dat slechts een fractie van het gemeten golfveld wordt gebruikt voor het afbeelden. In dit proefschrift presenteren we een methode, genaamd full wavefield migration (FWM), waarbij multiples in de data worden gebruikt om de belichting van de ondergrond te verbeteren op die plekken waar de primaries niet komen, om de resolutie te verbeteren dankzij een grotere apertuur en om artefacten in de migratie wegens interferentie van multiples te onderdrukken.

Dit proefschriflt toont de haalbaarheid van full wavefield migration aan voor een type boorgat seismiek die vertical seismic profiling (VSP) wordt genoemd. We weten dat bij de huidige praktijk, de afbeeldingen op basis van VSP data altijd lijden onder slechte illuminatie en kleine apertuur effecten. Om deze reden verwachten we dat bij een VSP acquisitie, multiples kunnen leiden tot een significante verbetering van de illuminatie, zowel in het reservoir als buiten de omgeving van het boorgat. In dit proefschrift is het voordeel van het gebruik van multiples in full wavefield migration aangetoond. We hebben de werking van ons algoritme bevestigd met 2D synthetische data en field VSP data.

Full wavefield migration is gesteld als een invers probleem, waarbij de reflectiviteit van de ondergrond de te schatten parameters zijn. We beschrijven een iteratief voorwaarts model, full wavefield modeling, die gebruikt wordt in het inversieschema. Full wavefield modelling stelt ons in staat om het volledige golfveld (primaries en alle multiples) te berekenen in termen van geschatte reflectiviteiten. In het voorwaartse model gebruiken we de aanname dat er een scheiding van schalen is tussen de achtergrond migratiesnelheden die de een-wegs golfpropagatie bepaalt en het reflecitiviteitsmodel die de twee-wegs verstrooiing bepaalt. Het voorwaartse model omvat de niet-lineariteiten van het golfveld die veroorzaakt worden door reflectiviteiten, inclusief de transmissie effecten en meervoudige reflecties op alle diepteniveaus. Om het inverse probleem op te lossen hebben we

een iteratief conjugate-gradient schema gebruikt, wat een lokale optimisatiemethode is.

We laten ook een oplossing zien voor het afbeelden van blended source VSP data met FWM. Dankzij het afbeelden op basis van een inversie algoritme kunnen we elk willekeurig complexe bronveld gebruiken zonder de noodzaak voor een apart deblending (pre-processing) stap. Dit proefschrift introduceert de concepten van elastische full wavefield modeling en inversie. Het elastisch modelleren van P en S golven wordt geïllustreerd voor een horizontaal gelaagd medium met een VSP geometrie. Het elastisch afbeelden van hoekafhankelijke reflectiviteitsparameters die mode-conversies in aardlagen omschrijven is een belangrijk onderwerp voor verder onderzoek.

Bijna-verticale structuren zoal zoutflanken vormen een uitdaging voor conventionele FWM. Wehebben het FWM algoritme ook uitgebreid om turning-waves te omvatten met behulp van horizontale een-wegs golfveld extrapolatie. Met deze uibreiding laten we zien dat FWM kan worden gebruik om steile of bijna-verticale structuren af te beelden met gebruik van het de turning-waves in de VSP data.

Alok Kumar Soni.

Acknowledgments

After finalizing this thesis, I would like to look back and acknowledge all the institutions or individuals who have helped me, influenced me or inspired me in my career progression so far. I would like to separately express my gratitude and my sense of belonging to all of them, as follows below:

Delphi consortium and TNW, Delft University of Technology: I still remember the day quite vividly - I had my interview held by professor Berkhout, professor Dries Gisolf and dr. Eric Verschuur during the Delphi meeting of June 2010. I knew that I am making the best decision of my career to join Delphi and felt privileged to get an opportunity to continue my PhD here. I would like to express my sincere thanks to professor Berkhout, professor Dries and dr. Eric for an enjoyable learning experience, which I will surely miss after I leave the group. The biggest source of inspiration is my supervisor Eric. As a legacy of Delphi, I am taking with me the memories of his technical help at all levels during my PhD, his prompt and practical solutions to any issue and an efficient management of the whole team. His positive outlook towards everything allows everyone in the group to produce the best out of them. Thanks again.

During my PhD, I had a chance to work closely with professor Berkhout too. For me he is a geophysics legend and every time I meet him, I am amazed by his enthusiasm and his innovative and revolutionary ideas. His advices on various stages of this research was indispensable for the positive outcomes. I also had a chance to learn from professor Dries Gisolf and dr. Gerrit Blacquière during this journey. I would like to thank my promotor professor Lucas van Vliet who took time to go through my thesis thoroughly and helped to improve it.

Next, I would like to express my thanks to all the PhD students with whom I had many learning and fun moments. I would like to mention most of the names here. Please consider it unintentional if I miss someone's name. Thanks Peter for helping me in my early days of PhD to get started, sharing the office with me and having many fun time together and always being an inspirational entrepreneur;

thanks Xander for many fruitful discussions, ideas and sharing experience towards developing FWM-JMI (the new imaging-inversion scheme) and for translating my PhD propositions and summary in Dutch; thanks Mikhail for various discussions on FWM and being a fun partner during our tough days of Dutch classes; thanks Gabrio for various mathematical discussions, sharing the office with me and for several cycling tours together; thanks Panos for helping me in my early days of PhD; thanks Amarjeet for sharing many fun and learning moments together during conferences and Delphi meetings in Houston. Many thanks are also due to other current and past members of our research group - Abdulrahman, Hannes, Matteo, Araz, Marwan, Khalid, Apostolos, Gabriel, Jan-Willem, Siddharth, Runhai, Bouchaib, Tomo, Yimin and Farid. I will remember all the pleasant outings, conferences and great dining I shared with you all guys. I wish the best to all of you.

I would like to express my special thanks to Edo and Henry for helping out the whole group during several computer or network related problems and also being a part of some enjoyable group excursions or conferences. Margaret, many thanks for your wonderful management and organizing all the small and big events successfully in our group. Also, I would always keep your good luck paper note you put once at my office desk during a tough time of my PhD. I would also like to thank all the sponsors of the Delphi consortium who support us financially and provide important feedback on our research on regular basis.

I know that I will leave Delphi group soon, however, in the future, I will comeback at some point of my career for research collaborations and more experiences with Delphi.

CiTG, Delft University of Technology: From CiTG, I would like to thank professor Wapenaar for his inspiring courses. Also, I would like to thank him for his critical remarks on this thesis to improve the contents.

Anadarko: I would like to thank John O'Brien from Anadarko to provide us a field walkaway VSP data from Gulf of Mexico and allow us to publish the results in this thesis.

Wintershall: I would like to thank Victor Petri, Paul Veeken, Richard Huisint-veld and Christian Hanitzsch from Wintershall to provide us a field walkaway VSP data from offshore Netherlands and test our algorithm.

Schlumberger: I would take an opportunity to thank my previous employer WesternGeco, Schlumberger, UK, where I worked from September 2006 to January 2011 as an imaging geophysicist. I would like to mention few names who helped me during my career progression during that period and beyond. Many thanks are due to Phil Whitfield, Kevin O' Sullivan, Dave Capper, Martin Dazley, Halim Roumane, Merigon Jarvis, Gavin Riley, Nigel Sayer, Gill Brown and John Matthewson for helping me in various stages during my job at Schlumberger. I

would also like to thank people from the research and development section who helped me to stay positive, think big and find a good school to do my research. Many thanks are due to David Hill, Dave Nichols, Shashi Menon, Dirk jan van Manen, Robin Fletcher, Kurt Eggenberger, Peter Vermeer, Ralf Ferber and Jorg Herwanger. I would also like to thank Robin Fletcher again for spending hours in sincerely reviewing my thesis thoroughly and provide critical advices to improve this thesis. Special thanks are due to Ed Kragh and James Rickett who invited me at Schlumberger Cambridge (Gould) Research UK to present my research work.

Shell: I would like to thank Fons ten Kroode to invite me at Rijswijk office to present my research work.

Dolphin Geophysical: I would like to thank Sergio Grion and Gareth Williams to invite me at UK office to present my research work.

PGS: I would like to thank Rolf Baardman, Gert-Jan and Roald van Borselen to invite me at Leiden office to present my research work.

My Schools in India: I would like to thank professor Pravin Gupta, professor Sri Niwas, professor S.K. Srivastava and Dr. Irene Sarkar from Indian Institute of Technology, Roorkee for their foundation lectures in applied geophysics during my masters, which always kept me interested in the subject. Also, I thank the Physics department at Hansraj College, University of Delhi for many fun and learning moments during my bachelors. Last but not least, I thank all the teachers at my home school - Pitts Modern School, Gomia, especially Pradeep Bansuri, Mahendra Patra, Jaswant Singh, S.D. Prasad and Thakur sir for their teachings during my high-school days.

Family: I dedicate this thesis to my parents and wife. Their best wishes and support kept me going ahead. I am living far from my parents since year 2000, and see them once in a year for some time. Their unconditional love and prolonged patience helped me all along my career. I would like to mention my other family members - my sisters Alka and Archana, Brother in-laws Rajesh and Vishwa, nieces Jasmine and Manya, and niece Nischay, who were always there for me in good and difficult times. Finally, I could not have finished happily without the support and love of my wife. I would like to thank my wife Aakanksha for sacrificing her own career in India and being with me in the Netherlands since one year, always being supportive and admiring me on all my small and big decisions. She helped me to work hard and enjoy life equally during this journey, which helped me to become more efficient at my work.

Old friends: I would like to remember some of my long-time friends whom I don't talk or meet every day but they always wish me good luck. Thank for being there - Pramod Kumar, Avneesh Singh, Ashok Kumar, Brijesh Singh, Ratnesh Pandey and Sandip Roy. And lastly, I wish Akash Kumar was here today with us to congratulate me. I miss you my friend.